

Contents

1	Introduction and Theory Overview	1
1.1	Introduction	1
1.2	Theory Overview	2
1.2.1	Heavy Vector Triplet Model	2
1.2.2	Basic Phenomenology	3
1.2.3	Explicit Models	8
2	The LHC and the CMS Detector	11
2.1	Large Hadron Collider	11
2.2	Compact Muon Solenoid	13
2.2.1	Tracker	15
2.2.2	ECAL	16
2.2.3	HCAL	17
2.2.4	Muon Chamber	19
2.2.5	Trigger System	20
3	Analysis Procedures	22
3.1	Monte Carlo Samples and Data sets	22
3.1.1	Signal MC	22
3.1.2	Background MC	24
3.1.3	Data Samples	24
3.2	Trigger	25
3.3	Physics Objects	26

3.3.1	Muon	26
3.3.2	Electron	29
3.3.3	Jet	33
3.3.4	Jet Grooming Algorithms	35
3.3.5	b-tagging	37
3.4	Pile-up reweighting	40
3.5	Event and Object selection	41
3.5.1	Lepton Requirements	41
3.5.2	Jet Requirement	41
3.5.3	Z boson Requirement	42
3.6	Data-MC comparison	44
3.7	Background Estimation	49
3.7.1	α ratio method	49
3.8	Signal Yields	50
3.8.1	signal efficiency	50
3.8.2	The m_{Zh} spectrum	51
3.8.3	The CSV distribution	53
3.9	Systematic uncertainties	56
4	Results and conclusion	60
4.1	Exclusion limit results	60
4.1.1	Counting result	60
4.1.2	1D shape result	61
4.1.3	2D shape result	61
4.2	Conclusion	61

List of Figures

1-1	Branching ratios as a function of the resonance mass for the HVT benchmark model A(left) and model B(right).	10
1-2	Theoretical production cross-section as a function of new resonance particles for HVT model B benchmark. Dash lines are 8 TeV predictions while solid lines are 13 TeV predictions.	10
2-1	Overview of the LHC and relative location of the detectors.	12
2-2	CERN accelerator complex.	13
2-3	Structure overview of the CMS detector.	14
2-4	Schematic layout of tracker.	15
2-5	The pixel detector inside tracker.	15
2-6	Schematic layout of the CMS ECAL.	17
2-7	Longitudinal view of one quarter of CMS and the location of HB (hadron barrel calorimeter), HE (hadron endcap calorimeter), HF (hadron forward calorimeter) and HO (hadron outer calorimeter)	18
2-8	Slice view of one quarter of muon chamber system.	20
2-9	CMS triggering and data acquisition architecture.	21
3-1	Feynman diagram for $Z' \rightarrow Zh \rightarrow 2l2q$	23
3-2	Example of the $E_{2\times 5}/E_{5\times 5}$ computation in the ECAL crystals. $E_{i\times j}$ is the energy contained in a $i \times j$ block around the seed crystal (defined as the highest deposit of the energy of the cluster).	32

3-3	Comparison of the jet mass in generic QCD events from the groomed jets divided by the jet mass of matched ungroomed jets for the three grooming techniques, for both data and the PYTHIA 6 Monte Carlo. [1] Events are collected with a single jet trigger.	36
3-4	[2] Distributions of (a) the secondary vertex multiplicity and (b) the CSV discriminator.	39
3-5	Number of vertices distributions after pile-up reweighting. Data are compared to the combination of all MC background samples. After reweighting, the distributions are almost identical to the data in both channels.	40
3-6	Z and Higgs p_T distribution are almost identical. We pick three samples with different mass points of Z' , 1000 GeV (red), 1500 GeV (blue) and 2000 GeV (green). These plots are made from the generator level signal samples without any proper selections.	42
3-7	Comparison between data and all background samples for two jet variables. The definition of muon/photon energy fraction is muon/photon energy divided by jet energy.	45
3-8	Charged electromagnetic/hadron energy fraction is defined by the ratio of the energy of charged particles in ECAL/HCAL to the jet energy. .	45
3-9	Neutral electromagnetic/hadron energy fraction is defined by the ratio of the energy of neutral particles in ECAL/HCAL to the jet energy. .	46
3-10	Comparison between data and MC in SB region using jet multiplicity (number of jets) and CA8jet transverse momentum.	46
3-11	Comparison between data and MC in SB region using CA8jet η and ϕ . .	47
3-12	Left: the prunedjet mass in the SB region. Right: the spatial distance between two subjets within the CA8jet.	47
3-13	Comparison between data and MC in SB region using mass and transverse momentum of reconstructed Z boson.	48
3-14	Comparison between data and MC in SB region using η and ϕ of reconstructed Z boson.	48

3-15	ΔR between the two selected leptons.	49
3-16	Left figure: the α ratio from MC simulation. Central figure: the m_{Zh} distribution observed from data SB. Right figure: the predicted m_{Zh} distribution in data signal region.	51
3-17	(a) The signal efficiencies plot of each Z' mass point. (b) Invariant mass distribution of the MC background simulation compared to the observed data and MC signal shape in the SR. (c) Normalized bin width m_{Zh} distribution (bin width/bin width of the first bin).	52
3-18	The CSV distribution comparison between data and MC samples in SR. .	54
3-19	The combined 2D shape result of data and MC background in SR. . .	54
3-20	The combined 2D shape result in SR of 800 GeV and 1000 GeV signal MC samples.	55
3-21	The combined 2D shape result in SR of 1500 GeV and 2000 GeV signal MC samples.	55
3-22	SR m_{Zh} distributions for both signal (1500 GeV) and background MC samples. The uncertainty of jet energy scale is shown as the green error band ($\pm 1\sigma$), while the error bar presents the statistic error.	56
3-23	(a) shows the distributions of number of vertices in electron channel, comparing central value of the total background prediction and the $\pm 1\sigma$ variation, and data as well. (b) shows the result in muon channel. .	57
3-24	The comparison between different PDF sets using m_{Zh} spectrum and CSV variable.	59
4-1	Observed and expected (with $\pm 1(2)\sigma$ band) 95% C.L. upper limit on $\sigma \times \text{BR}(Z' \rightarrow Zh)$ including all statistical and systematics uncertainties. .	62

List of Tables

3.1	Signal samples used in the analysis.	23
3.2	Background samples used in the analysis.	24
3.3	Data sets used in this analysis.	25
3.4	Summary of the muon ID selection criteria.	28
3.5	Summary of the modified HEEPv4.1 electron ID.	32
3.6	Event and object selection requirements used in the analysis.	43
3.7	Binning of the Zh invariant mass range.	50
3.8	The recommend selection from BTV group for boosted Higgs decay. If the ΔR between the two subjets within CA8jet larger than 0.3, applying CSVL selection on both subjets. If $\Delta R_{subjets} < 0.3$, applying CSVL on the CA8jet. In this analysis, we use the overall CSV distributions instead of selecting events by this variable (Modified). Note that, only leading CA8jet (the Higgs candidate) and subjets within it are considered in this strategy.	53
3.9	Data to simulation scale factors for muon and electron identification requirements in various p_T and η ranges.	58

¹ Chapter 1

² Introduction and Theory Overview

³ 1.1 Introduction

⁴ This thesis presents the analysis details and the results of the search for heavy reso-
⁵ nances decaying into a Z boson and a Higgs boson (h) at the center-of-mass energy of
⁶ 8 TeV, using 19.7 fb^{-1} p-p collision data. In turn, the Z boson is identified through
⁷ its leptonic decays (leptons often refer to e and μ only in experiments. $l = e, \mu$). The
⁸ Higgs boson h is expected to hadronically decay into a pair of b-quarks. The investi-
⁹ gated final states consist of two charged leptons which are identified in the detector
¹⁰ and limit the presence of the background, and two b-quarks from the hadronic Higgs
¹¹ decay which collects the largest possible fraction of Higgs events.

¹² This thesis is organised as follows. In the latter part of this chapter, the model that
¹³ predicts heavy resonances is introduced, including the expected cross section and the
¹⁴ specification of model parameters. In chapter 2, the LHC and the CMS experiment
¹⁵ are described, including the information of each sub-detector and the trigger system
¹⁶ of the CMS. The details of the analysis are shown in chapter 3. This chapter reveals
¹⁷ the way to reconstruct physical objects in CMS. By adding some proper kinematic
¹⁸ selections on those physics objects, the interested events in data collected by the CMS
¹⁹ detector can be selected. Moreover, this chapter shows the comparison between data
²⁰ and simulation. In the last chapter, the results of the search and the conclusion are
²¹ presented.

22 1.2 Theory Overview

23 Although the Higgs boson discovered by the ATLAS and CMS collaborations [3–5]
 24 imposes strong constraints on theories beyond the Standard Model(SM), the extreme
 25 fine tuning in quantum corrections required to have a light fundamental Higgs boson
 26 with mass close to 125 GeV [6–9] suggests that the Standard Model may be incom-
 27 plete, and not valid beyond a scale of a few TeV. Various dynamical electroweak
 28 symmetry breaking scenarios which attempt to solve this naturalness problem, such
 29 as Minimal Walking Technicolor [10], Little Higgs [11–13], or composite Higgs mod-
 30 els [14–16] predict the existence of new resonances decaying to a vector boson plus a
 31 Higgs boson.

32 1.2.1 Heavy Vector Triplet Model

33 Resonance searches are typically not sensitive to all the details and the free parameters
 34 of the underlying model, but only to those parameters or combinations of parameters
 35 that control the mass of the resonance and the interactions involved in its production
 36 and decay. Therefore, one can employ a simplified description of the resonance de-
 37 fined by a phenomenological Lagrangian where only the relevant couplings and mass
 38 parameters are retained. This model-independent strategy applies a Heavy Vector
 39 Triplet (HVT) [17] to the Standard Model group and reproduces a large class of ex-
 40 plicit models. In Eq. (1.1), the mathematical form of the simplified Lagrangian is
 41 defined, where V_ν^a , $a = 1,2,3$, is a real vector with vanishing hypercharge in the ad-
 42 joint representation of $SU(2)_L$, it describes one charged and one neutral heavy spin-1
 43 particle with charge eigenstate fields, and $D_{[\mu} V_{\nu]}^a$ represents the covariant derivative.

$$\begin{aligned} \mathcal{L}_V = & -\frac{1}{4} D_{[\mu} V_{\nu]}^a D^{[\mu} V^{\nu]}_a + \frac{m_V^2}{2} V_\mu^a V^{\mu a} \\ & + ig_V c_H V_\mu^a H^\dagger \tau^a \overset{\leftrightarrow}{D}^\mu H + \frac{g^2}{g_V} c_F V_\mu^a \sum_f \bar{f}_L \gamma^\mu \tau^a f_L \\ & + \frac{g_V}{2} c_{VVV} \epsilon_{abc} V_\mu^a V_\nu^b D^{[\mu} V^{\nu]}_c + \text{quadrilinear terms} \end{aligned} \quad (1.1)$$

$$V_\mu^\pm = \frac{V_\mu^1 \mp i V_\mu^2}{\sqrt{2}}, \quad V_\mu^0 = V_\mu^3 \quad (1.2)$$

$$D_{[\mu} V_{\nu]}^a = D_\mu V_\nu^a - D_\nu V_\mu^a, \quad D_\mu V_\nu^a = \partial_\mu V_\nu^a + g \epsilon^{abc} W_\mu^b V_\nu^c \quad (1.3)$$

$$H = \begin{pmatrix} \phi^+ \\ \phi^- \end{pmatrix} = \begin{pmatrix} \frac{1}{\sqrt{2}}(\phi_1 + i\phi_2) \\ \frac{1}{\sqrt{2}}(\phi_3 + i\phi_4) \end{pmatrix} \quad (1.4)$$

⁴⁴

⁴⁵ In these models, new heavy vector bosons (V^\pm, V^0) that couple to the SM Higgs
⁴⁶ doublet (Eq. 1.4) and SM gauge bosons with the parameters c_H and g_V and to the
⁴⁷ fermions via the combination $(g^2/g_V)c_F$. The parameter g_V represents the strength
⁴⁸ of the new vector boson interaction, while c_H and c_F represent the couplings to the
⁴⁹ Higgs and the fermions respectively, and are expected to be of the order of unity in
⁵⁰ most models.

⁵¹ 1.2.2 Basic Phenomenology

⁵² Masses and Mixings

After electro-weak symmetry breaking (EWSB), the only massless state is photon, which can be identified as the gauge field associated with the unbroken $U(1)_{em}$. The two other neutral mass eigenstates are the SM Z boson and one heavy vector of mass M_0 which are obtained by diagonalizing the mass matrix of the (Z, V^0) system by a rotation with angle θ_N

$$\begin{pmatrix} Z \\ V^0 \end{pmatrix} \rightarrow \begin{pmatrix} \cos \theta_N & \sin \theta_N \\ -\sin \theta_N & \cos \theta_N \end{pmatrix} \begin{pmatrix} Z \\ V^0 \end{pmatrix}. \quad (1.5)$$

The mass matrix is

$$\mathcal{M}_N^2 = \begin{pmatrix} \hat{m}_Z^2 & c_H \xi \hat{m}_Z \hat{m}_V \\ c_H \xi \hat{m}_Z \hat{m}_V & \hat{m}_V^2 \end{pmatrix}, \text{ where } \begin{cases} \hat{m}_Z = \frac{e\hat{v}}{2\sin\theta_W \cos\theta_W} \\ \hat{m}_V^2 = m_V^2 + g_V^2 c_{VVHH} \hat{v}^2 \\ \xi = \frac{g_V \hat{v}}{2\hat{m}_V} \end{cases}. \quad (1.6)$$

In the above equations \hat{v} denotes the Vacuum Expectation Value (VEV) defined by $\langle H^\dagger H \rangle = \hat{v}^2/2$, and one should know the masses \hat{m}_Z and \hat{m}_V do not coincide with the physical Z boson and the masses of the new resonances of this model, although they do in the approximations later (Eq. 1.12). The mass eigenvalues and the rotation angles are easily obtained by inverting the relations

$$\begin{aligned} Tr[\mathcal{M}_N^2] &= \hat{m}_Z^2 + \hat{m}_V^2 = m_Z^2 + M_0^2, \\ Det[\mathcal{M}_N^2] &= \hat{m}_Z^2 \hat{m}_V^2 (1 - c_H^2 \xi^2) = m_Z^2 M_0^2, \\ \tan 2\theta_N &= \frac{2c_H \xi \hat{m}_Z \hat{m}_V}{\hat{m}_V^2 - \hat{m}_Z^2}. \end{aligned} \quad (1.7)$$

- ⁵³ Note that M_0 represents the real mass eigenvalue of the neutral heavy vector boson.
- ⁵⁴ Moreover, since we assume $\hat{m}_V > \hat{m}_Z$, the only variable controls the sign of the
- ⁵⁵ tangent function is c_H , which is model dependent. Once the sign of c_H is determined,
- ⁵⁶ the tangent can be uniquely inverted.

The situation is similar in the charged vector mass matrix of (W^\pm, V^\pm) system, and M_\pm denotes the real mass eigenvalue of charged states as well.

$$\mathcal{M}_C^2 = \begin{pmatrix} \hat{m}_W^2 & c_H \xi \hat{m}_W \hat{m}_V \\ c_H \xi \hat{m}_W \hat{m}_V & \hat{m}_V^2 \end{pmatrix}, \text{ where } \hat{m}_W = \frac{e\hat{v}}{2\sin\theta_W} = \cos\theta_W \hat{m}_Z, \quad (1.8)$$

where it is diagonalized by

$$\begin{aligned} Tr[\mathcal{M}_C^2] &= \hat{m}_W^2 + \hat{m}_V^2 = m_W^2 + M_\pm^2 , \\ Det[\mathcal{M}_C^2] &= \hat{m}_W^2 \hat{m}_V^2 (1 - c_H^2 \xi^2) = m_W^2 M_\pm^2 , \\ \tan 2\theta_C &= \frac{2c_H \xi \hat{m}_W \hat{m}_V}{\hat{m}_V^2 - \hat{m}_W^2} . \end{aligned} \quad (1.9)$$

By checking Eq. (1.6) and Eq. (1.8), the charged and neutral mass matrices are connected by custodial symmetry, which can be shown in full generality to imply

$$\mathcal{M}_C^2 = \begin{pmatrix} \cos \theta_W & 0 \\ 0 & 1 \end{pmatrix} \mathcal{M}_N^2 \begin{pmatrix} \cos \theta_W & 0 \\ 0 & 1 \end{pmatrix} . \quad (1.10)$$

By taking the determinant of the above equation, or equivalently by comparing the charged and neutral determinants in Eq. (1.7) and Eq. (1.9), we obtain a generalized custodial relation among the physical masses

$$m_W^2 M_\pm^2 = \cos^2 \theta_W m_Z^2 M_0^2 . \quad (1.11)$$

From the simple formula above, we can start to identify the physically reasonable region of the parameter space in this model. We aim at describing new vectors with masses at or above the TeV scale, but we also want the SM masses $m_{W,Z} \sim 100$ GeV to be reproduced. Therefore we require a hierarchy in the mass relation of SM Z and W bosons versus the new vectors.

$$\frac{\hat{m}_{W,Z}}{\hat{m}_V} \sim \frac{m_{W,Z}}{M_{\pm,0}} \leq 10^{-1} \ll 1 \quad (1.12)$$

Use the limit above, we can expand the determinant formulas both in Eq. (1.7) and Eq. (1.9) to obtain simple approximations for m_W and m_Z

$$\begin{aligned} m_Z^2 &= \hat{m}_Z^2 (1 - c_H^2 \xi^2) (1 + \mathcal{O}(\hat{m}_Z^2 / \hat{m}_V^2)) , \\ m_W^2 &= \hat{m}_W^2 (1 - c_H^2 \xi^2) (1 + \mathcal{O}(\hat{m}_W^2 / \hat{m}_V^2)) . \end{aligned} \quad (1.13)$$

The parameter ξ can be either very small or of order unity. Both cases are realized in explicit models. While $\xi \ll 1$ is the most common situation, $\xi \sim 1$ only occurs in strongly coupled scenarios at very large g_V . In these approximations, SM tree-level experimental observation can be reproduced to percent accuracy.

Since $\hat{m}_W = \cos \theta_W \hat{m}_Z$, the W - Z mass ratio is thus given by

$$\frac{m_W^2}{m_Z^2} \simeq \cos^2 \theta_W . \quad (1.14)$$

Eq. (1.14) has one important implication on the masses of the new vectors. When combined with the custodial relation Eq. (1.11), it tells us that the charged and neutral V s are practically degenerate

$$M_{\pm}^2 = M_0^2(1 + \mathcal{O}(\%)) , \quad (1.15)$$

⁵⁷ In the following, when working at the leading order in the limit Eq. (1.12), we can
⁵⁸ ignore the mass splitting and denote the mass of the charged and the neutral states
⁵⁹ collectively as M_V . It is easy to check that in that limit $M_V = \hat{m}_V$.

⁶⁰ Decay Widths

Because of the hierarchy in the mass matrices, the mixing angles are naturally small. By looking at Eqs. (1.7), (1.9) and (1.12) we can estimate

$$\theta_{N,C} \simeq c_H \xi \frac{\hat{m}_{W,Z}}{\hat{m}_V} \leq 10^{-1} , \quad (1.16)$$

and after rotating to the mass basis, the coupling of the neutral and charged resonances to left- and right-handed fermion chiralities can be written in a compact form

for each fermion species $F = \{l, q, 3\}$.

$$\begin{cases} g_L^N = \frac{g^2}{g_V} \frac{c_F}{2} \cos \theta_C + (g_L^Z)_{SM} \sin \theta_N \simeq \frac{g^2}{g_V} \frac{c_F}{2} , \\ g_R^N = (g_R^Z)_{SM} \sin \theta_N \simeq 0 \\ g_L^C = \frac{g^2}{g_V} \frac{c_F}{2} \cos \theta_C + (g_L^W)_{SM} \sin \theta_C \simeq \frac{g^2}{g_V} \frac{c_F}{2} , \\ g_R^C = 0 \end{cases} \quad (1.17)$$

In the above equation $(g_{L,R}^{W,Z})_{SM}$ denote the ordinary SM W and Z couplings (with the normalization given by $g_L^W = g/\sqrt{2}$).

Given that the rotation angles are small, the couplings further simplify, as also shown in the equation. We could see that V interact mainly with left-handed chiralities and that all the couplings for each fermion species are controlled by the parameter combination $g^2/g_V c_F$. This gives tight correlations among different channels

$$\Gamma_{V_\pm \rightarrow f\bar{f}} \simeq 2\Gamma_{V_0 \rightarrow f\bar{f}} \simeq N_C[f] \left(\frac{g^2 c_F}{g_V}\right)^2 \frac{M_V}{48\pi}, \quad (1.18)$$

where $N_C[f]$ is the number of colors (3 for the di-quark and 1 for the dilepton decays). The parameters $c_F = \{c_l, c_q, c_3\}$ control the relative BRs to leptons, light quarks and the third family.

In the case of di-boson decay width

$$\begin{aligned} \Gamma_{V_0 \rightarrow W_L^+ W_L^-} &\simeq \Gamma_{V_\pm \rightarrow W_L^\pm Z_L} \simeq \frac{g_V^2 c_H^2 M_V}{192\pi} \frac{(1 + c_H c_{VVV} \xi^2)^2}{(1 - c_H^2 \xi^2)^2} = \frac{g_V^2 c_H^2 M_V}{192\pi} [1 + \mathcal{O}(\xi^2)], \\ \Gamma_{V_0 \rightarrow Z_L h} &\simeq \Gamma_{V_\pm \rightarrow W_L^\pm h} \simeq \frac{g_V^2 c_H^2 M_V}{192\pi} \frac{(1 - 4c_{VVH} \xi^2)^2}{1 - c_H^2 \xi^2} = \frac{g_V^2 c_H^2 M_V}{192\pi} [1 + \mathcal{O}(\xi^2)]. \end{aligned} \quad (1.19)$$

⁶¹ Note that Eq. (1.19) is derived in the Equivalent Gauge [18] because the decay to transverse SM vectors is highly suppressed while to the longitudinal parts grows with the energy of the process, therefore the Unitary Gauge which is used in the original

⁶⁴ Lagrangian is instead useful. The channels that are not shown in the above equations
⁶⁵ are either forbidden or suppressed like the decays to transverse polarizations.

⁶⁶ From this section, a very simple picture emerges. At small ξ , all the decay widths
⁶⁷ are fixed with a given resonance mass M_V and the couplings $\{g^2 c_F/g_V, g_V c_H\}$ which
⁶⁸ control the BRs in all relevant channels. Parameters c_{VVV} , c_{VHH} and c_{VW} are
⁶⁹ basically irrelevant. Thus, the basic phenomenology of this model is well described
⁷⁰ by a good approximation.

⁷¹ 1.2.3 Explicit Models

Now the general picture is clear, we can get exact values of the widths and BRs from explicit models. Consider two benchmark models, A and B, which correspond to two explicit models describing the heavy vectors in Refs. [19] and [14] respectively. All the c parameters are fixed to specific values in these models and the only free parameters are the resonance mass M_V and coupling g_V . Moreover, model A is inspired by weakly coupled extensions of the SM gauge group while model B is by strongly coupled scenarios of EWSB, *i.e.* Composite Higgs models, we will consider them in different regions of g_V , relatively small $g_V \leq 3$ and relatively large $g_V \geq 3$.

Figure 1-1 shows the BRs as functions of the mass in model A and B. As expected from the previous discussion and according to Refs. [19], model A predicts

$$c_H \simeq -g^2/g_V^2, c_F \simeq 1, \\ g_V^2 c_H^2 \simeq g^4 c_F^2/g_V^2 \simeq g^2/g_V. \quad (1.20)$$

Therefore Eq. (1.18) and (1.19) can be determined in the following form for V_0 in model A ($g_V = 1$),

$$\Gamma_{V_0 \rightarrow f\bar{f}'} \simeq N_c[f] \frac{g^4 M_V}{96\pi} \\ \Gamma_{V_0 \rightarrow W^+W^-} \simeq \Gamma_{V_0 \rightarrow Zh} \simeq \frac{g^4 M_V}{192\pi}. \quad (1.21)$$

One can easily check either from the plot or the equation, a factor of two difference comparing the BRs between fermions and bosons. Due to the color factor, leptons and quarks also have a difference by a factor of three. Since the c_F term is universal both in A and B. The total width in model A decreases with increasing g_V because of the overall suppression (g^2/g_V) in Eq. (1.20).

On the contrary, in model B the c_H term is unsuppressed

$$c_H \simeq c_F \simeq 1 , \\ g_V^2 c_H^2 \simeq g_V^2 , g^2 c_{c_F} / g_{g_V} \simeq g^2 / g_V . \quad (1.22)$$

Thus the determinate V_0 decay widths for model B ($g_V = 3$) are

$$\Gamma_{V_0 \rightarrow f\bar{f}'} \simeq N_c[f] \frac{g^4 M_V}{342\pi} \\ \Gamma_{V_0 \rightarrow W^+W^-} \simeq \Gamma_{V_0 \rightarrow Zh} \simeq \frac{3M_V}{64\pi} . \quad (1.23)$$

- ⁷² For model B _{$g_V=3$} the dominant BRs are into di-bosons and the fermionic decays are
- ⁷³ extremely suppressed. Moreover, the total width increases with increasing g_V since it
- ⁷⁴ is dominated by the di-boson width which grows with g_V as expected from Eq. (1.22).
- ⁷⁵ This model B is particularly interesting for the present search, since it predicts signal
- ⁷⁶ cross sections of the order of fb [17] [20] [Fig. 1-2], branching ratios to vector bosons
- ⁷⁷ close to unity, and thus being accessible at the LHC. In the latter chapters, the mass
- ⁷⁸ eigenstate of the neutral heavy vector boson in model B scenario refers to the Z'
- ⁷⁹ particle, which is the search target of this thesis.

⁸⁰

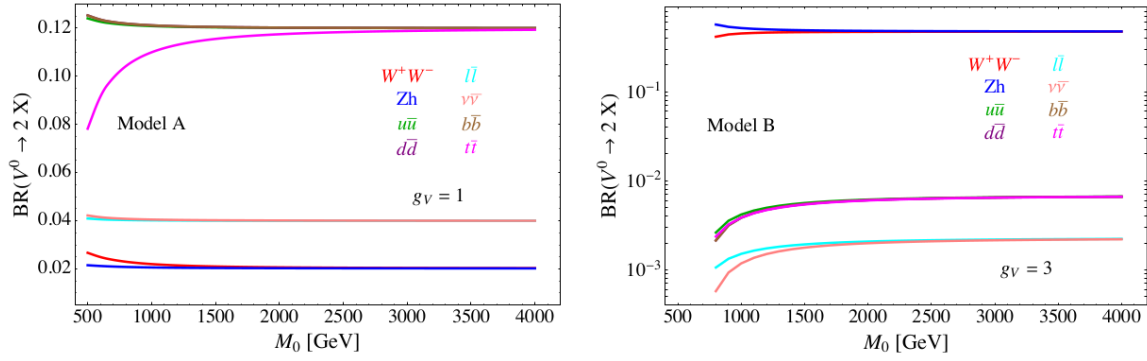


Figure 1-1: Branching ratios as a function of the resonance mass for the HVT benchmark model A(left) and model B(right).

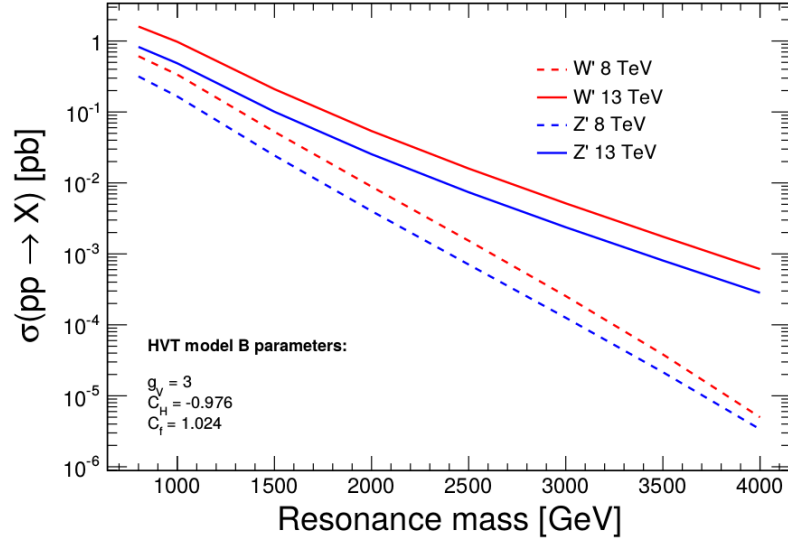


Figure 1-2: Theoretical production cross-section as a function of new resonance particles for HVT model B benchmark. Dash lines are 8 TeV predictions while solid lines are 13 TeV predictions.

81 **Chapter 2**

82 **The LHC and the CMS Detector**

83 This thesis is based on the data collected by the Compact Muon Solenid (CMS)
84 detector at the Large Hadron Collider (LHC). CMS is one of the two largest detectors
85 built at the LHC. This chapter will briefly introduce the LHC and the CMS detector.

86 **2.1 Large Hadron Collider**

87 The LHC is the world’s most powerful hadron collider and the largest experimental
88 facility ever. It was built by the European Organization for Nuclear Research (CERN)
89 between 1998 and 2008 in collaboration with over 10,000 scientists and engineers from
90 over 100 countries, as well as hundreds of universities and laboratories. It lies in a
91 tunnel of 27 km in circumference, as deep as 175 m beneath the France–Switzerland
92 border near Geneva. The designed maximum collision energy and highest luminosity
93 of the LHC are 14 TeV and $10^{-34}\text{cm}^{-2}\text{s}^{-1}$, respectively.

94 Other accelerators that had been originally built at CERN for previous experi-
95 ments serve as an injection chain for the LHC now (Fig. 2-2). The proton beam starts
96 from LINAC, a small linear accelerator, where the energy of protons first reaches at
97 50 MeV. The proton beam then passes through a booster and goes to the PS, where
98 it is accelerated up to 25 GeV. After that, it reaches 450 GeV in the SPS. The beam
99 is finally injected in the LHC ring from the SPS, and it had been accelerated up to
100 4 TeV in 2012. In early 2015, the proton beam had been accelerated to 6.5 TeV, a

101 value near its designed energy, before undergoing collision.

102 There are four collision points at the LHC, corresponding to four main experiments, CMS, ATLAS, LHCb and ALICE. The ALICE experiment is optimized to
103 study heavy-ion (Pb-Pb nuclei) collisions and focusing on the physics of strongly
104 interacting matter at extreme energy densities. LHCb is a specialized b-physics ex-
105 periment, measuring the parameters of CP violation in the interactions of b-hadrons.
106 Such studies can help to explain the matter-antimatter asymmetry of the universe.
107 Last, CMS and ATLAS are two general purpose detectors. The aims of these two
108 experiments are investigating a wide range of physics, including the search for the
109 beyond standard model particles, extra dimensions, and dark matter.
110



Figure 2-1: Overview of the LHC and relative location of the detectors.

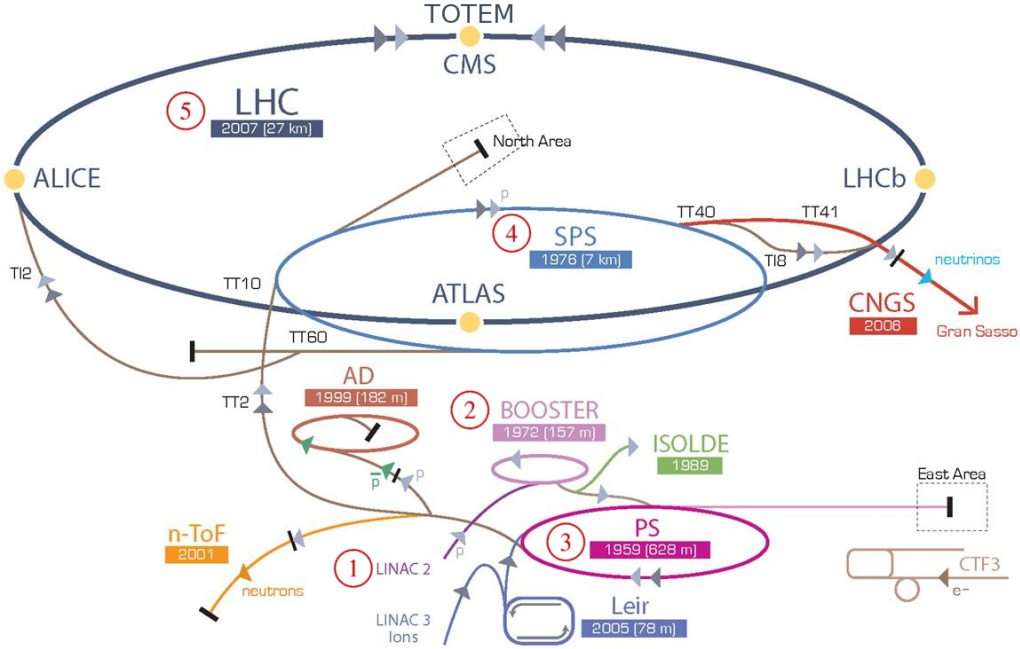


Figure 2-2: CERN accelerator complex.

2.2 Compact Muon Solenoid

The Compact Muon Solenoid (CMS) is designed to cope very high rate of interactions expected to take place at the high LHC luminosity. It has the typical structure of detectors at hadron colliders: a central region (*barrel*) enclosed by two disks (*endcaps*). The structure of CMS can be seen in Fig. 2-3.

Solenoid and Sub-detectors

CMS features a powerful superconducting coil, generating a solenoidal magnetic field around 3.8 Tesla in a large volume which hosts different sub-detectors. The magnetic field lines close through steel yoke in the outer region. The distinct sub-detectors are designed in order to obtain the highest possible resolution and the largest acceptance for every kind of particles.

The innermost layer is a silicon-based tracker. Surrounding it is a scintillating crystal electromagnetic calorimeter (ECAL), which is itself surrounded with a sampling calorimeter for hadrons (HCAL). The tracker and the calorimeters are compact

125 enough to fit inside the CMS Solenoid. Outside the magnet are the large muon
126 chambers.

CMS Detector

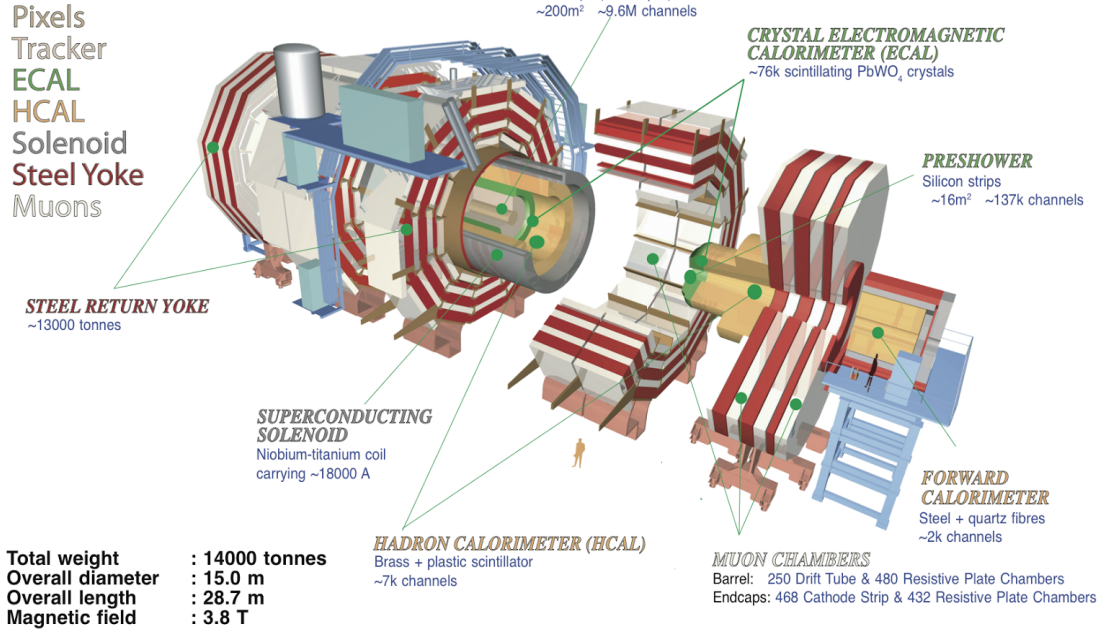


Figure 2-3: Structure overview of the CMS detector.

127 Coordinate System

128 The CMS coordinate system is oriented such that the x -axis points to the center of
129 the LHC ring, the y -axis points vertically upward and the z -axis is in the direction
130 of the beam. The azimuthal angle ϕ is measured from the x -axis in the $x - y$ plane
131 and the radial coordinate in this plane is denoted by r . The polar angle θ is defined
132 in the $r - z$ plane, while the pseudo-rapidity $\eta = -\ln \tan(\theta/2)$. The momentum
133 component transverse to the beam direction, denoted by p_T , is computed from the x -
134 and y -components, and the transverse energy is defined as $E_T = E \sin \theta$.

¹³⁵ 2.2.1 Tracker

¹³⁶ Tracker is the most inner part of CMS that records the productions of collisions in the
¹³⁷ first place. It traces the charged particles' trajectories. Physicists can reconstruct the
¹³⁸ vertices of the interaction and the momentum of charged particles by linking tracks
¹³⁹ to the collider's pipe and measuring the curves of particles under magnetic field.

¹⁴⁰ The tracking system is composed of two kinds of detector, the pixel detector and
¹⁴¹ silicon strip detector. The pixel detector is built from three barrel layers at $r = 44$,
73, 102 mm, and two endcap disks on each side at $z = \pm 345, \pm 465$ mm.

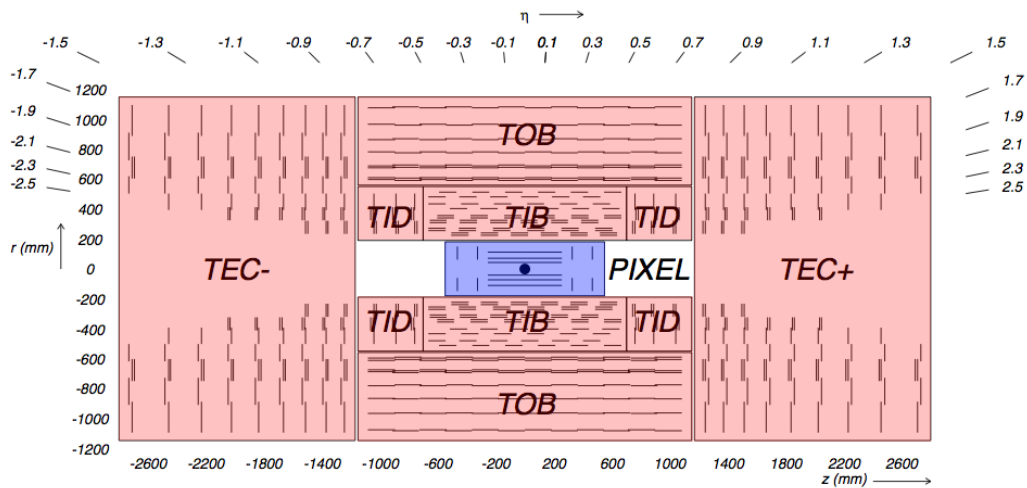


Figure 2-4: Schematic layout of tracker.

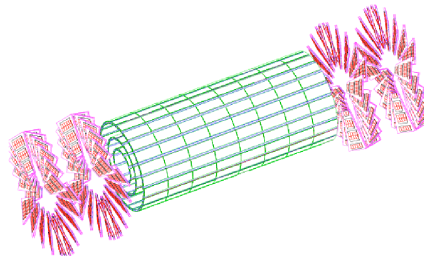


Figure 2-5: The pixel detector inside tracker.

¹⁴² The pixel detector, though about the size of a shoebox, consists of 1440 segmented
¹⁴³ silicon sensor modules with total 66 million readout channels. Charge carriers are
¹⁴⁴ distributed over several pixels. The analog pulse height information can be used
¹⁴⁵ to identify different particle types.

146 to calculate the center of certain charge distribution which could improve the hit
147 information. The spatial resolution is measured to be about $10 \mu\text{m}$ for the $r - \phi$
148 plane or about $20 \mu\text{m}$ for z direction measurement.

149 Outside the pixel detector, there comes the silicon strip detector. The barrel
150 region of silicon strip detector is divided into two parts, the Tracker Inner Barrel
151 (TIB) and the Tracker Outer Barrel (TOB). The former is composed of four layers
152 of silicon sensors with a thickness of $320 \mu\text{m}$ and of strip pitches varying from 80
153 to $120 \mu\text{m}$. The TOB is made of six layers. In this kind of sub-detector, thicker
154 silicon sensors ($500 \mu\text{m}$) are employed, while the strip pitch varies from 120 to 180
155 μm . The endcap region ($|\eta| > 1.6$) is covered by the Tracker Inner Disks (TID)
156 and the Tracker End Cap (TEC). The entire silicon strip detector is comprised of
157 15200 high-sensitivity modules consisting of detecting unit, supporting structure and
158 readout electronic system.

159 2.2.2 ECAL

160 The Electromagnetic Calorimeter (ECAL) measures the energy of photons, electrons
161 and positrons. It it is placed just outside the tracker, but still inside the solenoid.
162 ECAL is made of 74848 lead-tungstate (PbWO_4) crystals. This material is charac-
163 terized by a high density (8.28 g/cm^3), which gives the crystals a very compact form
164 and makes them particularly suitable to be placed inside the magnetic coil. Another
165 reason, this material has also a fast temporal response ($\sim 10 \text{ ns}$) and its radiation
166 length (X_0) of 0.89 cm give ECAL the possibility to fully contain the expansion of
167 the electromagnetic shower.

168 The arrangement of ECAL is shown in Fig. (2-6). The barrel crystals have a front
169 face area of $2.2 \times 2.2 \text{ cm}^2$ and a length of 23 cm. They are positioned at $r = 1.29$
170 m in pseudo-rapidity region $0 < |\eta| < 1.479$. The crystals in the endcaps have a
171 $2.47 \times 2.47 \text{ cm}^2$ front face, a 22 cm length and they are positioned at $z = 3.17 \text{ m}$ in
172 $1.479 < |\eta| < 3.0$. A Preshower detector is placed in front of the endcaps crystals.
173 The active elements of Preshower are two planes of silicon strips with a pitch of 1.9
174 mm, which lie behind disks of lead absorber at depths of $2X_0$ and $3X_0$. It allows the

175 rejection of photon pairs from π^0 decays and improves the estimation of the direction
176 of photons, to enhance the measurement of the two-photon invariant mass.

The energy resolution of the ECAL is given by three different contributions [21]
(E in GeV),

$$\frac{\sigma_E}{E} = \frac{2.8\%}{\sqrt{E}} \oplus \frac{12\%}{E} \oplus 0.3\% \quad (2.1)$$

177 where the first term is statistical in nature, it also contains fluctuation in showering
178 and in the amplification through photodiodes, the second one considers electronic
179 noise and pile-up, the last term is mainly due to the calibration.

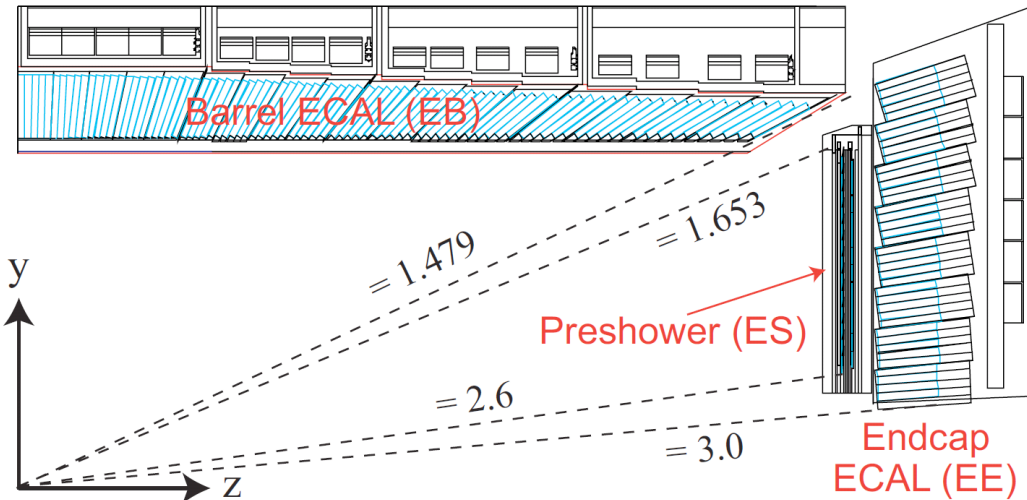


Figure 2-6: Schematic layout of the CMS ECAL.

180 2.2.3 HCAL

181 The hadron calorimeter (HCAL) is placed mainly between ECAL and the magnet
182 coil. It measures the energy of hadrons and mesons. Additionally it provides indirect
183 measurement of the presence of non-interacting, uncharged particles such as neutrinos.
184 The design is strongly influenced by these aims, hence an important requirement is the
185 high hermeticity (the ability to capture every particle emerging from the collisions).
186 This means the detector must cover the biggest possible portion of the solid angle.

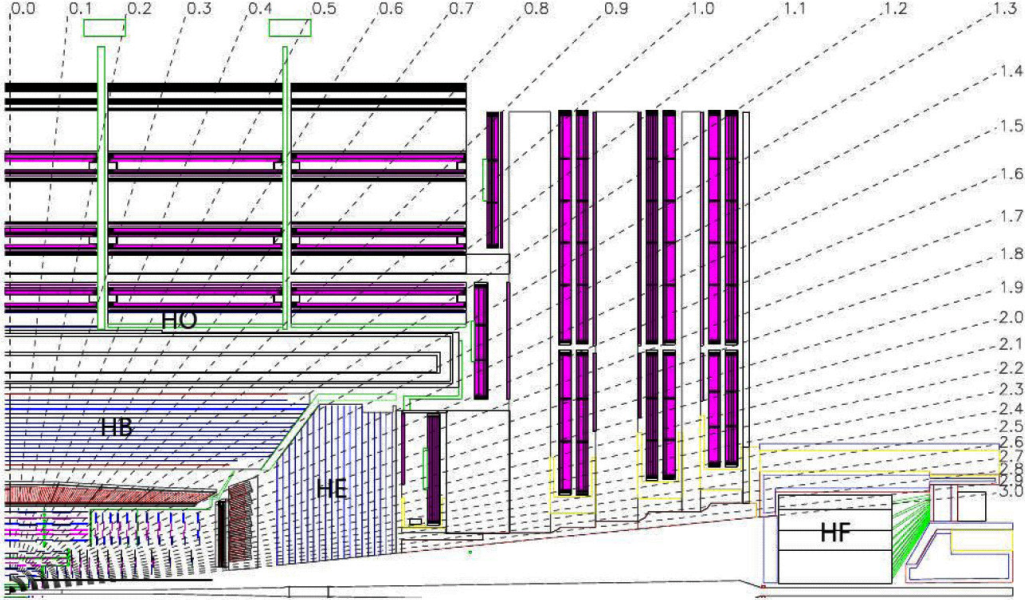


Figure 2-7: Longitudinal view of one quarter of CMS and the location of HB (hadron barrel calorimeter), HE (hadron endcap calorimeter), HF (hadron forward calorimeter) and HO (hadron outer calorimeter)

187 For this reason, a hadron forward calorimeter is required, which is placed outside
 188 the magnet return yokes, with a total coverage of $3 < |\eta| < 5.31$ at 11 m from the
 189 interaction point. Moreover, an outer hadronic calorimeter is placed in the first muon
 190 absorber layer in order to enhance the containment of high energy jets in the central
 191 region of the detector.

192 HCAL is a sampling calorimeter, whose active elements are plastic scintillators
 193 interleaved with brass absorber plates and read out by wavelength shifting fibers.
 194 Brass has been chosen as absorber material for its short interaction length and because
 195 it is non-magnetic. The thickness of the absorber layers is between 60 mm in the barrel
 196 and 80 mm in the endcaps. The barrel has 5.46 interaction lengths at $\eta = 0$ and 10.82
 197 at $\eta = 1.3$, while the endcaps have an average of 11 interaction lengths [22].

The HCAL energy resolution (E in GeV and measured by pion) [23] is

$$\frac{\sigma_E}{E} \simeq \frac{a}{\sqrt{E}} \oplus 5\% \quad (2.2)$$

198 where $a \simeq 65\%$ in the barrel, $a \simeq 85\%$ in the endcaps and $a \simeq 100\%$ in the HF.

199 **2.2.4 Muon Chamber**

200 The efficient detection of muons has primary importance, as muons represent a clear
201 signature for a large number of processes. Muons can penetrate several meters of
202 iron without interacting. Unlike most particles, they are not stopped by any of
203 calorimeters in CMS. Therefore, chambers to detect muons are placed at the very
204 edge of the experiment where they are the only particles likely to register a signal.

205 The muon system fulfills three purposes, muon identification, momentum mea-
206 surement and triggering. Three different types of gaseous detectors are used for CMS
207 muon system depending on the requirements.

208 **Drift Tube**

209 The drift tube (DT) system measures muon positions in the barrel part of the detector.
210 Each DT chamber, on average $2\text{ m} \times 2.5\text{ m}$ in size, consists of 12 aluminium layers,
211 arranged in three groups of four segmentations, each with up to 60 4-cm-wide tubes
212 that contain a stretched wire within each gas volume. The middle group measures
213 the coordinate along the direction parallel to the beam and the two outside groups
214 measure the perpendicular coordinate.

215 **Cathod Strip Chamber**

216 In the two endcaps, where the muon flux and the residual inhomogeneous magnetic
217 field are higher, cathode strip chambers (CSC) are used. CSC is composed of anode
218 wires and cathod strips in the gas volume. The chambers are arranged in 4 disks
219 perpendicular to the beam, and in concentric rings (3 rings in the innermost station,
220 2 in the others) in each of the endcaps.

221 **Resistive Plate Chambers**

222 Resistive plate chambers (RPC) are fast gaseous detectors that provide a muon trigger
223 system parallel with DTs and CSCs. Each RPC consists of two parallel plates, a

²²⁴ positively charged anode and a negatively charged cathode, both made of a very high
²²⁵ resistivity plastic material and separated by a gas volume.

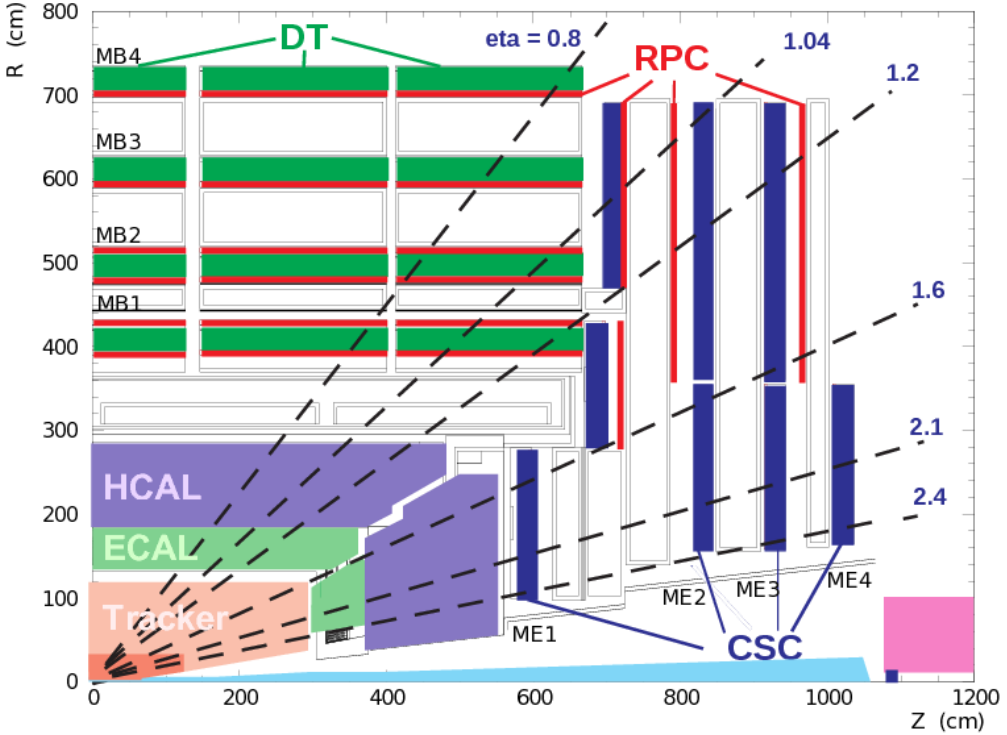


Figure 2-8: Slice view of one quarter of muon chamber system.

²²⁶ 2.2.5 Trigger System

²²⁷ To have a good chance of producing rare particles, a very large number of collisions
²²⁸ is required (LHC proton bunches collide every 25 ns). Most collision events in the
²²⁹ detector are soft and do not produce interesting events. The amount of data from
²³⁰ each crossing is approximately 1 megabytes, which at the 40 MHz crossing rate would
²³¹ result in 40 terabytes of data a second, an amount that the experiment cannot store.
²³² The task of the trigger system is to reduce the storage rate while keeping a high
²³³ efficiency on the potentially interesting events. In CMS the input rate is reduced in
²³⁴ two steps, Level-1 Trigger (L1T) and High-Level Trigger (HLT).

235 **Level-1 Trigger**

236 After the Level-1 Trigger selection, the event recording frequency is decreased to
237 100kHz [24], which is much smaller than the collision rate. The L1T objects are
238 particles (such as photons, muons and electrons), jet candidates, global transverse
239 energy and missing transverse energy. Level-1 Trigger just chooses the event with E_T
240 and P_T higher than the thresholds.

241 **High Level Trigger**

242 High Level Trigger is behind the readout buffers after Level-1 Trigger. It reduces
243 the data output rate to 100Hz by using all the information from CMS including the
244 sub-detectors. The reconstruction algorithms are the same as the off-line analysis.
245 However, the triggering procedure doesn't need maximal precision, therefore these
246 algorithms are modified to be faster even with lower resolution.

247

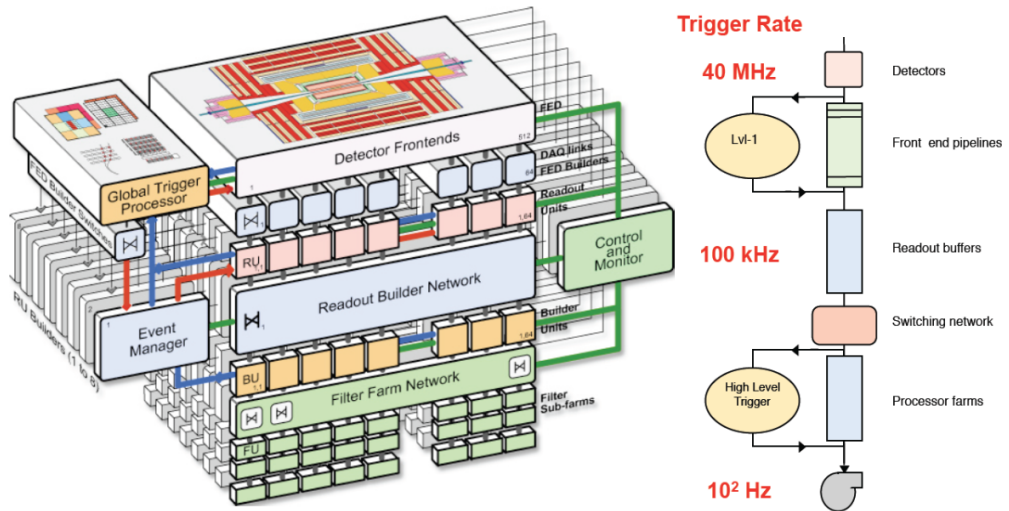


Figure 2-9: CMS triggering and data acquisition architecture.

²⁴⁸ **Chapter 3**

²⁴⁹ **Analysis Procedures**

²⁵⁰ In this chapter, the analysis procedures of the search for Z' decaying into Zh in $llbb$
²⁵¹ final state are reported. The data sets and Monte Carlo (MC) samples we used in this
²⁵² analysis will be indicated. Physics objects reconstruction and event selections are also
²⁵³ introduced. Moreover, background yields and the effects of systematic uncertainties
²⁵⁴ will be discussed in the end of this chapter.

²⁵⁵ **3.1 Monte Carlo Samples and Data sets**

²⁵⁶ **3.1.1 Signal MC**

²⁵⁷ As introduced in section 1.2.3, the signal hypothesis is HVT model B benchmark.
²⁵⁸ The heavy resonance (Z') is tested using a wide set of masses from 800 GeV to 2000
²⁵⁹ GeV, one masspoint every 100 GeV (Table 3.1). The signal is generated by Mad-
²⁶⁰ Graph5_aMC@NLOv5.2.2.1 [25] in LO mode, as a narrow spin-1 neutral resonance
²⁶¹ and is forced to decay in the $Z' \rightarrow Zh \rightarrow llqq$ channel. Showering and hadronization
²⁶² are performed with PYTHIA6 [26].

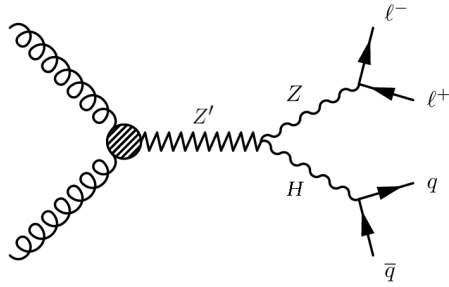


Figure 3-1: Feynman diagram for $Z' \rightarrow Zh \rightarrow 2l2q$.

Sample	Number of Processed Events	$\sigma_{LO}(\text{pb})$
ZPrime_ZH_lljj_M800-MADGRAPH	10710	0.00685367
ZPrime_ZH_lljj_M900-MADGRAPH	10209	0.00485861
ZPrime_ZH_lljj_M1000-MADGRAPH	19997	0.003263
ZPrime_ZH_lljj_M1100-MADGRAPH	9370	0.00217483
ZPrime_ZH_lljj_M1200-MADGRAPH	10710	0.00145484
ZPrime_ZH_lljj_M1300-MADGRAPH	9369	0.000979745
ZPrime_ZH_lljj_M1400-MADGRAPH	10497	0.000664783
ZPrime_ZH_lljj_M1500-MADGRAPH	19999	0.000454339
ZPrime_ZH_lljj_M1600-MADGRAPH	8950	0.000312541
ZPrime_ZH_lljj_M1700-MADGRAPH	9369	0.000216282
ZPrime_ZH_lljj_M1800-MADGRAPH	10708	0.000150398
ZPrime_ZH_lljj_M1900-MADGRAPH	10498	0.000105039
ZPrime_ZH_lljj_M2000-MADGRAPH	19999	7.36377e-05

Table 3.1: Signal samples used in the analysis.

263 **3.1.2 Background MC**

264 Since we are looking for new resonances decaying in semi-leptonic final state, the
265 background samples of this analysis are originated by all SM events with two leptons
266 and at least one jet as final state. The dominant background contribution is the
267 produciton of Z boson with jets. This Z+jets sample is produced by MADGRAPH.
268 In the matrix element level, the Z boson is forced to decay into two leptons, and
269 further this sample is divided into two samples depending on the Z p_T , higher than
270 100 GeV or between 70 and 100 GeV. The contribution of events with Z p_T less than
271 70 GeV is negligible due to further cut on the objects p_T in the selection criteria.

272 The second dominant source of background is $t\bar{t}$ production. Both of the two top
273 quarks decay into the final state (top decays into a W boson and a b quark first)
274 that gives two charged leptons, neutrinos and two b-jets. This sample is generated
275 by POWHEGv1 [27].

276 Other sources of background considered are SM di-boson productions (WW, WZ
277 and ZZ) generated by PYTHIA6. All the background samples are required to pass
278 phase-space cuts, $p_T^l > 60$ GeV and $60 < M_{ll} < 120$ GeV. Related statistics are reported
279 in Table 3.2.

Sample	Number of Processed Events	$\sigma_{NLO}(\text{pb})$
DYJetsToLL_PtZ-70To100	11764538	63.5
DYJetsToLL_PtZ-100	12511326	39.4
TTTo2L2Nu2B	10783509	25.8
WW	7759752	56.0
WZ	9910267	22.4
ZZ	9769891	7.6

Table 3.2: Background samples used in the analysis.

280 **3.1.3 Data Samples**

281 In this analysis, the full CMS data collected in 2012 are used, corresponding to the
282 integrated luminosity of 19.7 fb^{-1} at the center-of-mass energy $\sqrt{s} = 8$ TeV. For each
283 lepton channel, there are four datasets. All datasets are collected with a double muon

or a double electron trigger, as explained in detail in the next section. The trigger algorithm employed for the electron samples doesn't use any information from the tracker but only the energy deposite in the ECAL. This expedient is implemented in order to avoid any possible inefficiencies due to the presence of two tracks very close to each other when the Z is highly boosted and its decay products are very collimated. Such a trigger is contained in the Photon/DoublePhotonHighPt dataset.
 The full dataset names are listed in Table 3.3.

AOD Sample	Luminosity (pb^{-1})
DoubleMu/Run2012A-22Jan2013-v1	876.225
DoubleMuParked/Run2012B-22Jan2013-v1	4409
DoubleMuParked/Run2012C-22Jan2013-v1	7017
DoubleMuParked/Run2012D-22Jan2013-v1	7369
Photon/Run2012A-22Jan2013-v1	876.225
DoublePhotonHighPt/Run2012B-22Jan2013-v1	4412
DoublePhotonHighPt/Run2012C-22Jan2013-v1	7055
DoublePhotonHighPt/Run2012D-22Jan2013-v1	7369

Table 3.3: Data sets used in this analysis.

3.2 Trigger

Since the final state contains two leptons of the same flavour and at least one jet, we perform this analysis on the DoubleMu and Photon/DoublePhotonHighPt datasets.
 The first dataset is triggered by two muons, the second one is triggered by two eletrons.
 These triggers are:

- HLT_Mu22_TkMu8* (for DoubleMu datasets)
- HLT_DoubleEle33_*(for Photon/DoublePhontonHighPt datasets)

The muon trigger has a double p_T threshold, requires leading muon p_T greater than 22 GeV and sub-leading muon p_T greater than 8 GeV. Differently, the double electron trigger requires a higher threshold of 33 GeV on both electrons. The trigger efficiencies are close to 1 in both cases.

302 **3.3 Physics Objects**

303 **3.3.1 Muon**

304 **Reconstruction**

305 The muon reconstruction algorithm at CMS takes advantage of the redundancy of
306 detection methods. Muon tracks are first reconstructed independently in the inner
307 tracker (tracker track) and in the muon system (standalone track). Based on these
308 objects, two reconstruction approaches are used [28]:

309 • *Globol Muon* (outside-in): Starting from a standalone track, this algorithm
310 finds a best tracker track to match the standalone track. Then, the fit of the
311 track is repeated using the hits both in the tracker and in the muon system [29].
312 The resulting object is called a *Global Muon*. At large transverse momentum
313 ($p_t > 200$ GeV), the global muon fit can improve the momentum resolution
314 compared to the tracker-only fit.

315 • *Tracker Muon* (inside-out): A tracker muon is reconstructed using an opposite
316 direction of the direction for a global muon. In this approach, all tracker tracks
317 with $p_T > 0.5$ GeV and the total momentum $p > 2.5$ GeV are considered
318 as possible muon candidates. The extrapolation to the muon system takes
319 into account the magnetic field, average expected energy losses, and multiple
320 scattering in the detector material. If at least one muon segment matches the
321 extrapolated track, the corresponding track track qualifies as a *Tracker Muon*.
322 This algorithm is useful for low- p_T muons that do not fully penetrate the muon
323 system, and therefore only register a few hits.

324 If no match is found when extrapolating outside-in, the standalone track is stored
325 as a *Stanalone Muon*. This happens only for less than 1% of the muons produced in
326 a collison, and the reconstruction efficiency is about 99% for the muon which carries
327 enough high momentum within detector coverage [28].

328 **Identification**

329 We use both tracker muons and global muons in this analysis. To identify muons
330 from the signal, the muons must pass one of these two off-line selections, high- p_T
331 muon ID or tracker-based muon ID [30]. The requirements are listed as follows:

332

333 High- p_T muon ID

334 • Muon identified as a *Global Muon*.

335 • Number of muon hits in the global track > 0 .

336 • Number of matched muon stations > 1 .

337 • Number of pixel hits > 0 .

338 • Number of tracker layers with hits > 8 .

339 • Transverse impact parameter $d_{xy} < 0.2$ cm.

340 • Longitudinal impact parameter $d_z < 0.5$ cm.

341 • Relative error on the track transverse momentum $\sigma_{p_T}/p_T < 0.3$.

342

343 In the tracker-based muon ID, the muon has to be identified as a *Tracker Muon*,
344 and the requirement of muon hits in the global track is removed. Other requirements
345 are the same.

346 An additional useful variable for lepton identification is the isolation. It is defined
347 as the scalar sum of the p_T of the reconstructed objects within a cone (typical size is
348 $\Delta R = 0.3$, $\Delta R \equiv \sqrt{\Delta\eta^2 + \Delta\phi^2}$) space around the lepton track but excluding the p_T
349 of the lepton itself. Moreover, the relative isolation is defined as isolation divided by
350 the lepton p_T ($I_{rel} = Iso/p_T^{lept}$). The relative isolation is more frequently used in the
351 modern analysis.

352 In this analysis, a modified isolation criteria is used. The two muons originated
353 from boosted Z decay are close to each other, and consequently the presence of another

354 muon in the isolation cone could break the function of this variable. In order to solve
 355 this problem we use a tracker-based isolation relative quantity, explicitely removing
 356 the momentum flow from any other muon passing our muon selection. Moreover, a
 357 tracker-based isolation is well motivated also by two additional aspects: it is more
 358 independent of pile up (pile-up tracks tipically do not match the primary vertex)
 359 and does not include possible muon radiation. Finally, the modified requirement is
 360 $I_{rel}^{mod} < 0.1$.

361

Variable	High- p_T	Tracker-based
Muon type	Global muon	Tracker muon
Muon hits in global track	≥ 1	-
Muon stations matched	≥ 2	≥ 2
d_{xy}	< 0.2 cm	< 0.2 cm
d_z	< 0.5 cm	< 0.5 cm
Pixel hits	≥ 1	≥ 1
Tracker layers	≥ 8	≥ 8
σ_{p_T}/p_T	< 0.3	< 0.3
I_{rel}^{mod}	< 0.1	< 0.1

Table 3.4: Summary of the muon ID selection criteria.

362 **3.3.2 Electron**

363 **Reconstruction**

364 Electrons are reconstructed from energy deposits in the ECAL matched to tracks
365 reconstructed in the silicon tracker. They have less distinguishable signatures than
366 muons in the detector due to the jet-induced background in ECAL. Therefore, to
367 reconstruct an election, it's essential to find a brilliant way to match the infomation
368 acquired in both tracker and ECAL.

369 **Clustering**

370 For every single hit from an electron in ECAL, approximately 94% of energy is con-
371 tained in 3×3 crystals and 97% in 5×5 crystals. To form a cluster, crystals with
372 $E_T > 1$ GeV is picked as seeds. Then starting from seed crystal, dominos of size 1×3
373 or 1×5 are created in $\eta - \phi$ plane. If the energy of these dominos exceed 0.1 GeV
374 threshold, thus added up the energy of dominos along the ϕ direction.

375 Moreover, the effects of conversion process and bremsstrahlung radiation must be
376 taken into account to reconstruct the electron energy more precisely. The concept
377 of electron superclustering is to collect the energy of photons from bremsstrahlung
378 radiation along the ϕ direction with fixed η width of the seed crystal. The technical
379 details of the supercluster can be found in [31].

380 **Tracking**

381 There are several steps to reconstruct electron tracks in CMS experiment. The hit
382 on the pixel and the tracker are reconstructed in the first step. The second step is
383 to find the seed of tracks by matching at least two hits in pixel detector. Lst step
384 is to fit the trajetory starting from the seed. To perform this fit, the Gaussian-sum
385 filter (GSF) algorithm is used [32]. In GSF algorithm, the energy loss probability
386 density function is constructed by multiple Gaussian functions. Finally, the electrons
387 are built by matching the superclusters to the GSF tracks. Reconstruction efficiencies

388 for electrons $E_T > 20$ GeV are generally above 95% in EB and 90% in EE [33].

389 Identification

390 The electron identification used in this analysis is based on HEEPv4.1 [34]. As what
391 we did for the muon id, we need to modify the isolation definition again because of
392 the small ΔR between two electrons. The requirements are listed as follows:

393

394 Modified HEEPv4.1 electron ID

- 395 • Transversal supercluster energy > 40 GeV.
- 396 • Pseudorapidity of supercluster $|\eta_{\text{SC}}| < 1.442$ for barrel electrons, or $1.556 <$
397 $|\eta_{\text{SC}}| < 2.5$ for endcap electrons.
- 398 • Have either $E_{2\times 5}/E_{5\times 5} > 0.94$ or $E_{1\times 5}/E_{5\times 5} > 0.83$.

399 • Ratio of HCAL deposit energy to ECAL deposit energy (Fig. 3-2) smaller than
400 0.5.

- 401 • Number of inner layer lost hits smaller than 2.
- 402 • Have $|d_{xy}| < 0.02$ cm for barrel electrons, or $|d_{xy}| < 0.05$ cm for endcap electrons.

403

404 As what we did for the muon id, by the same reason we need to modify the
405 isolation definition again. In this case there are three isolation variables that have to
406 be changed.

- 407 • Modified track isolation is required be to lower than 5 GeV. This variable is
408 defined as the scalar p_T sum of the tracks within a $\Delta R = 0.3$ cone around
409 the electron, and excluding the p_T of another electron which passes the above
410 selections and its track is inside the cone.
- 411 • The electromagnetic calorimeter isolation I_{ECAL} is defined as the scalar sum
412 of E_T of the crystals in a $\Delta R = 0.3$ cone around the particular electron (an

413 inner area of full-width 3 crystal), excluding a 4 crystals width around any other
414 electron. The dimension of the ECAL crystals corresponds roughly at $\Delta R \sim$
415 0.01 to 0.02. The threshold of I_{ECAL} is varying with the electron transverse
416 energy.

- 417 • The hadronic calorimeter isolation I_{HCAL} is defined as the scalar sum of E_T
418 of the HCAL caloTowers with a center in a $\Delta R = 0.3$ cone around the elec-
419 tron, excluding those lying within $\Delta R = 0.15$ of the electron itself and of any
420 other electron [35]. The threshold of this variable also varies with the electron
421 transverse energy.

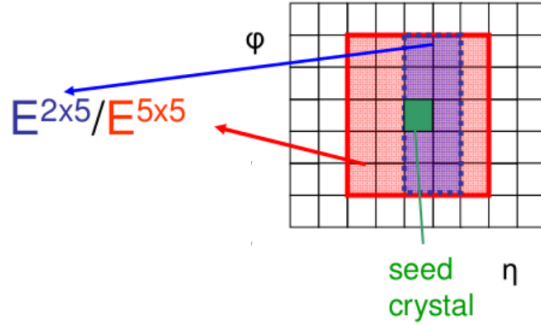


Figure 3-2: Example of the $E_{2\times 5}/E_{5\times 5}$ computation in the ECAL crystals. $E_{i\times j}$ is the energy contained in a $i \times j$ block around the seed crystal (defined as the highest deposit of the energy of the cluster).

Variable	Barrel	Endcap
E_T	$> 40 \text{ GeV}$	$> 40 \text{ GeV}$
$ \eta_{SC} $	$ \eta_{SC} < 1.442$	$1.556 < \eta_{SC} < 2.5$
H/E	< 0.05	< 0.05
$E_{2\times 5}/E_{5\times 5}$	> 0.94 or $E_{1\times 5}/E_{5\times 5} > 0.83$	-
Inner Layer Lost Hits	$<= 1$	$<= 1$
$ d_{xy} $	$< 0.02 \text{ cm}$	$< 0.05 \text{ cm}$
Iso_{Trk}^{mod}	$< 5 \text{ GeV}$	$< 5 \text{ GeV}$
$Iso_{Ecal,Hcal}^{mod}$	$< 2 \text{ GeV} + 0.03E_T$	$< 2.5 \text{ GeV for } E_T < 50 \text{ GeV}$ $< 2.5 \text{ GeV} + 0.03E_T \text{ for } E_T > 50 \text{ GeV}$

Table 3.5: Summary of the modified HEEPV4.1 electron ID.

422 **3.3.3 Jet**

423 Since gluons and quarks cannot exist in free state due to the color confinement
424 [36], they fragment into hadrons. The result of this fragmentation (or called the
425 "hadronization") is a jet of particles depositing energy in the detectors.

426 **Reconstruction**

427 Jet clustering algorithms are among the main tools for analyzing data from hadronic
428 collisions. In this section, an extensively used clustering algorithm called "sequential
429 recombination algorithm" [37,38] will be introduced. At first, events are reconstructed
430 using the particle flow algorithm (PF) [39], which attempts to identify and measure all
431 the stable particles in a collision by combining information from all the sub-detectors.
432 The PF algorithm categorizes all particles into five types: muons, electrons, photons,
433 charged and neutral hadrons. The resulting particle flow candidates are passed to
434 the anti- k_T (AK) [37] or Cambridge/Aachen (CA) [38,40] jet clustering algorithms to
435 create jets (AK and CA are two commonly used branches of sequential recombination
436 algorithms).

437 The jet clustering algorithms are implemented as follows:

$$d_{iB} = p_{T,i}^{2p}$$
$$d_{ij} = \min(p_{T,i}^{2p}, p_{T,j}^{2p}) \frac{\Delta R_{i,j}^2}{R^2} \quad (3.1)$$

438 In Eq. (3.1), the pair of objects (i , j) denote two input candidate particles to
439 the algorithm. ΔR_{ij} ($\Delta R_{ij} \equiv \sqrt{\Delta\eta_{ij}^2 + \Delta\phi_{ij}^2}$) is the spatial distance between the two
440 objects, and R is the typical cone size of the jet. The parameter p corresponds to
441 different categories of algorithms and will be introduced in the later paragraph.

442 The clustering proceeds by comparing the value of the two quantities, d_{iB} and d_{ij} .
443 If $d_{ij} > d_{iB}$, the algorithm will look for another possible combination of (i , j). If
444 $d_{ij} < d_{iB}$, the 4-momentum of object i will merge into j, and then the object j forms a

445 pseudo-jet, but the algorithm will not stop looking for a new object until all particles
446 are clustered into jet.

447 The parameter p can be chosen as follows:

448 • $p = 0$: Cambridge/Aachen algorithm;

449 • $p = -1$: Anti- k_T algorithm;

450 The difference between CA/AK algorithms is clear, CA algorithm is only consid-
451 ering the spatial distance of the two candidate objects (if $\Delta R_{ij} < R$, merged). In the
452 case of anti- k_T algorithm, p_T of the object presents as a weight for the distance.

453 The anti- k_T algorithm has better energy calibration, while the CA algorithm was
454 found to be more efficient at finding hard subjets within the jets in simulation-based
455 studies [41]. Therefore the CA jets are used in this analysis to identify events con-
456 taining hadronically-decaying Higgs bosons.

457 Identification

458 As discussed in the previous section, this analysis use the Cambridge/Aachen algo-
459 rithm with a cone radius of $R = 0.8$ for the identification of jets (CA8 jets). Further-
460 more, jets are required to pass the following loose identification criteria [42, 43]:

461

462 Loose JetID ($> 99\%$ efficiency)

463 • Muon energy fraction smaller than 0.99

464 • Photon energy fraction smaller than 0.99

465 • Charged electromagnetic energy fraction smaller than 0.99

466 • Neutral hadron energy fraction smaller than 0.99

467 • Charged hadron energy fraction larger than 0

468 • Number of constituent particles larger than 1

469 For all jet candidates, $|\eta| < 2.4$ requirement are also applied.

470 **3.3.4 Jet Grooming Algorithms**

471 The jet mass is the main observable in distinguishing a boson-jet from a QCD jet. Jet
472 grooming aims to suppress underlying events and pile-up radiation from the target jet,
473 and improves the discrimination by pushing the jet mass for QCD jets towards lower
474 values while maintaining the jet mass for boson-jets around the boson-mass [44, 45].

475 Typically three different grooming algorithms are considered, trimming [46], fil-
476 tering [47] or pruning [48, 49]. Studies of these different grooming methods in CMS
477 are presented in [50].

478 • **Trimming algorithm:** Trimming is a technique that ignores subjets (smaller
479 jets formed by the breakup of a larger one) below a minimum p_T fraction thresh-
480 old within the original jet. Trimming reclusters the jet's constituents with a
481 smaller radius R_{sub} . Then accepts only the subjets that have $p_{T,frac} > f_{cut}$,
482 where the $p_{T,frac}$ is defined as subjet p_T devideed by the original jet p_T , and
483 f_{cut} is typically taken proportional to H_T , the scalar sum of the p_T of all jet
484 reconstructed in the event.

485 • **Filtering algorithm:** Filtering reclusters jet constituents with smaller radius
486 R_{filt} , and sorts the subjets in order of their p_T . The final jet is thus redefined as
487 the sum of the four-momentum of the n hardest subjets. By default the factor
488 is n=3, but it's not a fixed number, n depends on the analysis.

489 • **Pruning algorithm:** The idea is to take a jet of interest and then to reclus-
490 ter it using a sequential clustering algorithm for vetoing soft and large-angle
491 recombinations between pseudojets i and j.

Clustering proceeds as explained in the previous section, but it is vetoed if the
candidates are too far away in ΔR .

$$\text{veto if } \Delta R_{ij} > r_{cut} \times 2m/p_T \quad (3.2)$$

And the energy sharing is too asymmetric.

$$\text{veto if } z_{ij} = \frac{\min(p_{T,i}, p_{T,j})}{p_{T,i+j}} < z_{cut} \quad (3.3)$$

Where z_{cut} and r_{cut} are parameters of the algorithm (default value: $z_{cut} = 0.1$, $r_{cut} = 0.5$). If both these conditions are satisfied the softer one of the two candidate is not considered.

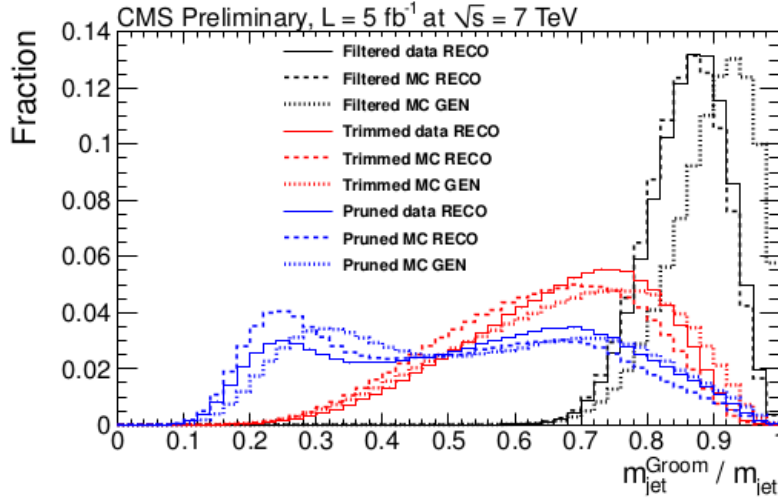


Figure 3-3: Comparison of the jet mass in generic QCD events from the groomed jets divided by the jet mass of matched ungroomed jets for the three grooming techniques, for both data and the PYTHIA 6 Monte Carlo. [1] Events are collected with a single jet trigger.

As shown in Fig. 3-3, the filtering algorithm is the least aggressive grooming technique, with groomed jet masses close to the original case. The trimming algorithm is moderately aggressive which produces a much wider final mass distribution. Pruning is the most aggressive tecniqe and a bimodal distribution begins to appear.

In cases where the pruned jet mass is small, jets usually have most of their energy configured in core components with little gluon radiation, which leads to narrow jets. Instead, when the pruned jet mass is large, the jets are split more symmetrically and more similar with the boson-jet structure. In this analysis we use the pruned jet mass because of its capability to improve the jet mass resolution and background rejection.

501 **3.3.5 b-tagging**

502 b-tagging [2, 51] is an algorithm to identify jets originating from b-quarks. It is an
503 important component in analyses searching for new physics. Particularly challenging
504 are those involving top quark or Higgs boson production with decays in the boosted
505 regime.

506 The methods for b-tagging are based on the unique features of b-jets: B-hadrons
507 have sufficient lifetime that they can travel some distance before they decaying. On
508 the other hand, their lifetimes are not so high as those of light quark hadrons, so they
509 decay inside the detector rather than escape. Another characteristic is, the bottom
510 quark is much more massive than anything it decays into. Thus its decay products
511 tend to have higher transverse momentum. This causes b-jets to be wider, have
512 higher multiplicities and invariant masses, and also to contain low-energy leptons
513 with momentum perpendicular to the jet.

514 There have different approaches of b-tagging algorithm described in [2]. In this
515 analysis, a complex approach we used will be introduced in the next section.

516 **Identification using Combined Secondary Vertex**

517 Combined Secondary Vertex (CSV) algorithm is a complex approach involves the
518 information of secondary vertices and track-based lifetime. In order to enhance b
519 purity, a secondary vertex must meet the following requirements:

- 520 • secondary vertices must share less than 65% of their associated tracks with
521 the primary vertex and the significance of the radial distance between the two
522 vertices has to exceed 3σ ;
- 523 • secondary vertex candidates with a radial distance of more than 2.5 cm with
524 respect to the primary vertex, with masses compatible with the mass of K^0
525 or exceeding $6.5 \text{ GeV}/c^2$ are rejected, reducing the contamination by vertices
526 corresponding to the interactions of particles with the detector material and by
527 decays of long-lived mesons;

- 528 • the flight direction of each candidate has to be within a cone of $\Delta R < 0.5$
529 around the jet direction.

530 There are also requirements to the tracks that forms the primary vertex, the detail
531 reconstruction method and selections are in [2]. After all selections, the following set
532 of variables with high discriminating power and low correlations is used to build
533 likelihood functions:

- 534 • the vertex category (real, "pseudo" or "no vertex");
535 • flight distance significance in the transverse plane ("2D");
536 • the vertex mass;
537 • number of tracks at the vertex;
538 • ratio of the energy carried by tracks at the vertex with respect to all tracks in
539 the jet;
540 • pseudorapidities of the tracks at the vertex with respect to the jet axis;
541 • the 2D IP (impact parameter) significance of the first track that raises the
542 invariant mass above the charm threshold of $1.5 \text{ GeV}/c^2$ (tracks are ordered
543 by decreasing IP significance and the mass of the system is recalculated after
544 adding each track);
545 • the number of tracks in the jet;
546 • the 3D IP significances for each track in the jet.

547 Two likelihood ratios are built from these variables. They are used to discriminate
548 between b and c jets and between b and light-parton jets. They are combined with
549 prior weights of 0.25 and 0.75, respectively. The combined value is the CSV discrimi-
550 nator. By using these additional variables, the CSV algorithm provides discrimination
551 also in cases when no secondary vertices are found, increasing the maximum efficiency
552 with respect to the other algorithms (in the "no vertex" category only the last two

variables in the set are available). The distributions of the vertex multiplicity and of the CSV discriminator are shown in Fig. 3-4.

555

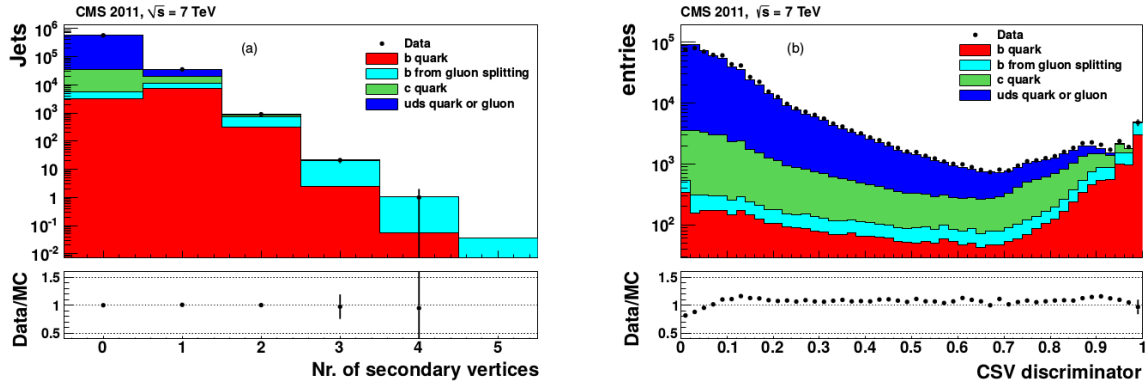


Figure 3-4: [2] Distributions of (a) the secondary vertex multiplicity and (b) the CSV discriminator.

556 3.4 Pile-up reweighting

557 At the typical luminosity provided by the LHC, it is common to reconstruct more than
 558 one vertex per event. The main event vertex is defined as the one with the highest
 559 sum of the p_T^2 of the associated tracks. The presence of additional interactions, known
 560 as pile-up (PU).

561 The simulation generates the pile-up roughly to match the condition in data,
 562 however there are still difference between the pile-up numbers in data and MC. It is
 563 neccesary to reweight pile-up distribtuions of MC samples to match the data more
 564 precisely. By applying a proper weight to each MC event according to the pile-up
 565 distribution from data, the MC samples can describe the data better. Fig. 3-5 shows
 566 the number of vertices after pile-up reweighting in both two lepton channel.

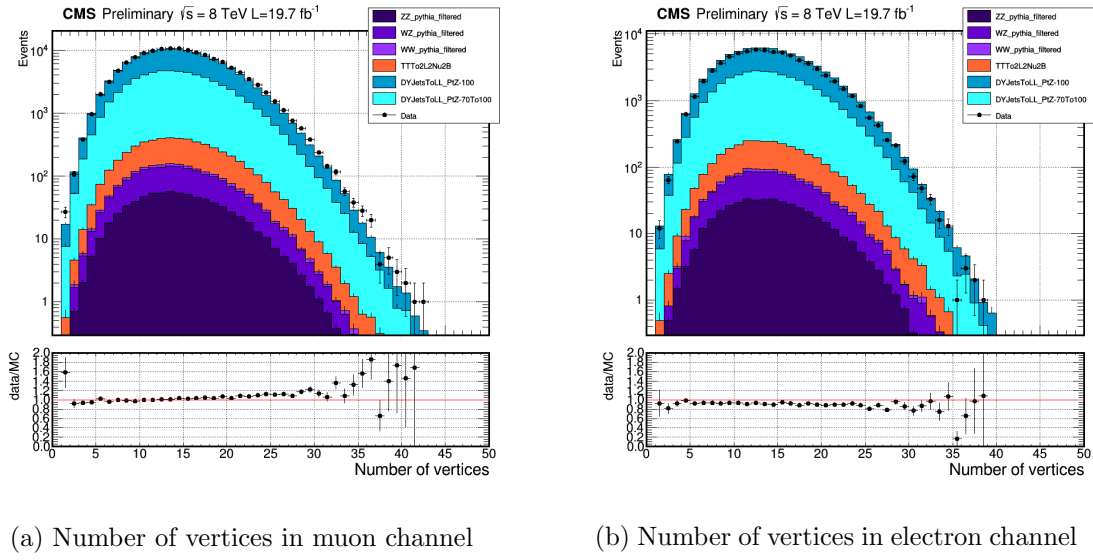


Figure 3-5: Number of vertices distributions after pile-up reweighting. Data are compared to the combination of all MC background samples. After reweighting, the distributions are almost identical to the data in both channels.

567 **3.5 Event and Object selection**

568 **3.5.1 Lepton Requirements**

569 **Muon Selection**

570 Besides the muon ID criteria discussed in section 3.3.1 (Table 3.4), we also require
571 kinematic cuts on the muon candidates. We require that the transverse momentum of
572 the leading muon candidate must be greater than 40 GeV, while the second leading
573 muon transverse momentum minimum threshold is 20 GeV. All muon candidates
574 must be in the pseudo-rapidity region of $|\eta| < 2.4$.

575 **Electron Selection**

576 Kinematic cuts on the electron candidates are also applied. Although the electron
577 ID selection (Table 3.5) already required the pseudo-rapidity of electron supercluster,
578 we cut on the $|\eta| < 2.5$ for electron candidates and all electrons must be outside
579 of [1.4442,1.566] in the η region to avoid the ECAL gap. The p_T requirement is a
580 bit different from the muon case. Since the HLT trigger already selects electron p_T
581 greater than 33 GeV, we require both leading and sub-leading electrons p_T greater
582 than 40 GeV in advance.

583 **3.5.2 Jet Requirement**

584 CA8jets in our signal process originate from Higgs decay. If the Z' mass is large
585 enough, the Higgs will be boosted. Therefore we require higher kinematic thresholds
586 to the CA8jets. In every event, there must be at least one CA8jet with $p_T > 80$ GeV,
587 $|\eta| < 2.4$, passing loose jet ID and the pruned-jet mass must be greater than 40 GeV
588 to remove jets from backgrounds.

589 Furthermore, in order to veto leptons that are mis-identified as jets, leptons overlap
590 with jets are removed by the ΔR cut, i.e. if there's a lepton passing all lepton
591 selections and the spatial distance to a CA8jet smaller than 0.1 ($\Delta R_{jet,lepton} < 0.1$),

592 then the jet will be removed.

593 3.5.3 Z boson Requirement

594 The Z boson candidate is reconstructed by adding four-momentum of the selected
 595 lepton pair. The Z boson mass is about 91 GeV, therefore we require the reconstructed
 596 invariant mass of the Z boson in the mass region [70 GeV, 110 GeV] where is ± 20
 597 GeV to its theoretical mass.

598 For the CA8jet from Higgs, we require a minimum p_T threshold of 80 GeV. Since
 599 the transverse momentum of Z' is zero and the mass difference between Z and Higgs
 600 is negligible ($1 \text{ TeV} >> 125 \text{ GeV} \sim 91 \text{ GeV}$), the Z and the Higgs boson are back to
 601 back at the transverse plane and their p_T 's are identical. Therefore we require the
 602 same minimum p_T threshold to the Z boson. Fig. 3-6 shows the transverse momentum
 603 distributions from the signal samples.

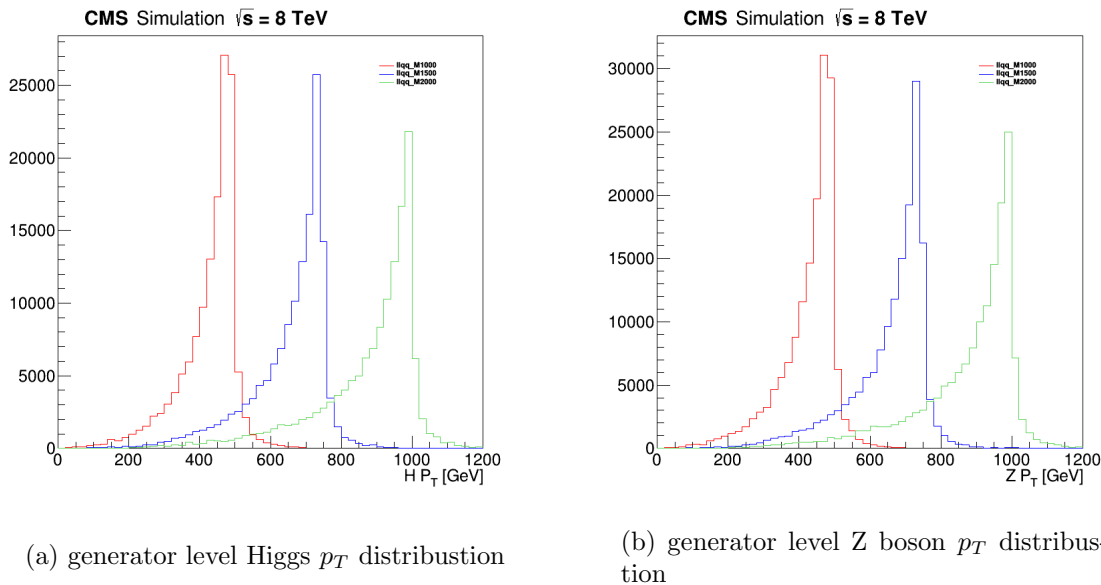


Figure 3-6: Z and Higgs p_T distribution are almost identical. We pick three samples with different mass points of Z' , 1000 GeV (red), 1500 GeV (blue) and 2000 GeV (green). These plots are made from the generator level signal samples without any proper selections.

604 Finally, all selection requirements are summarized in Table 3.6.

Selection	Value	Comments
Trigger	HLT_Mu22_TkMu8 HLT_DoubleEle33	DoubleMu dataset DoublePhoton dataset
Leading muon p_T	$p_T > 40$ GeV	
Sub-leading muon p_T	$p_T > 20$ GeV	
Muon η	$ \eta < 2.4$	
Muon ID	High p_T tracker based	
Muon isolation I_{trk}^{mod}	< 0.1	
Leading electron p_T	$p_T > 40$ GeV	
Sub-leading electron p_T	$p_T > 40$ GeV	
Electron η	$ \eta < 2.5$ out of [1.4442,1.566]	To avoid ECAL gap.
Electron ID	HEEP modified	
Electron isolation		
I_{trk}^{mod}	< 5 GeV	
$I_{ECAL,HCAL}^{mod}$	$< 2 \text{ GeV} + 0.03E_T$ $< 2.5 \text{ GeV}$ $< 2.5 \text{ GeV} + 0.03E_T$	Barrel for $E_T < 50$ GeV candidates in Endcap for $E_T > 50$ GeV candidates in Endcap
Jet ID	Loose working point	
Jet p_T	$p_T > 80$ GeV	
Jet η	$ \eta < 2.4$	
Prunedjet mass	> 40 GeV	
Veto jet-lepton overlap	$\Delta R_{jet,lepton} < 0.1$	Remove the jet satisfies this requirement.
Z p_T	$p_T > 80$ GeV	
Z mass window cut	$70 \text{ GeV} < m_Z < 110 \text{ GeV}$	

Table 3.6: Event and object selection requirements used in the analysis.

605 3.6 Data-MC comparison

606 In this section, a comparison between data and simulation is reported for various
607 kinematic observables. It can be seen that the dominant background contribution
608 comes from the Z+jets production, while sub-leading contributions are from $t\bar{t}$ and
609 dibosons can be negligible.

610 On top of the selections described in previous section, additional regions are de-
611 fined as following:

- 612 • **Signal region (SR):** Represents the phase space where the signal is expected,
613 defined by the prunedjet mass in $110 \text{ GeV} < m_{\text{prunedjet}} < 140 \text{ GeV}$ region. The
614 range is chosen by $\pm 15 \text{ GeV}$ to the mass of Higgs.
- 615 • **Sidebands (SB):** Defined by the interval between $70 \text{ GeV} < m_{\text{prunedjet}} <$
616 110 GeV . This region is signal-depleted. In our case, we don't consider pruned-
617 jet mass higher than 140 GeV , because of the poor statistics and the excessive
618 contribution of $t\bar{t}$ events.

619 In the following plots, the data-MC comparison is performed in SB region and
620 all background samples are weighted to the same luminosity as data. The results
621 combined both muon and electron channels. Because of the signal region in data is
622 considered **blind** in this analysis stage, so they are not shown.

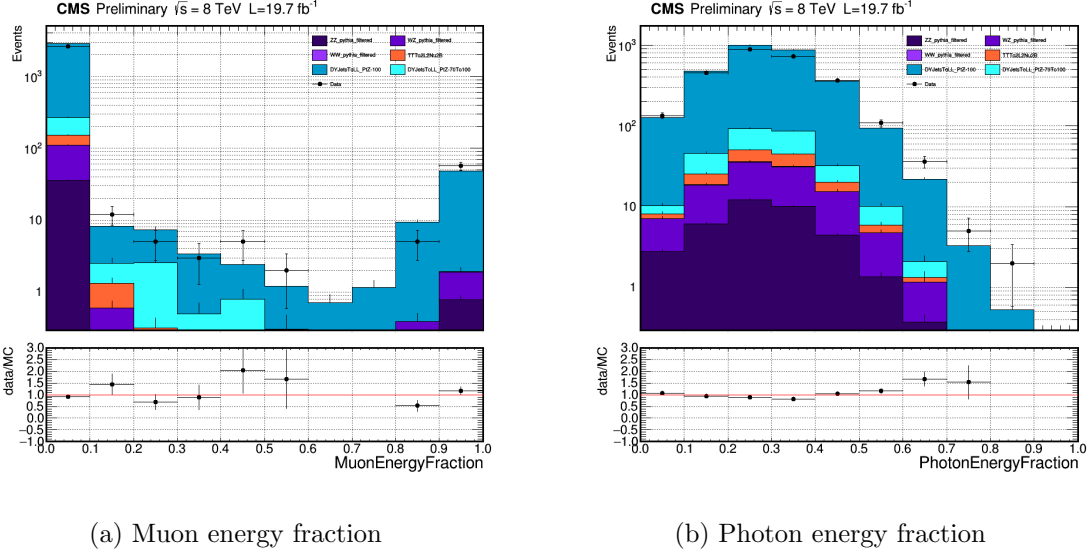


Figure 3-7: Comparison between data and all background samples for two jet variables. The definition of muon/photon energy fraction is muon/photon energy divided by jet energy.

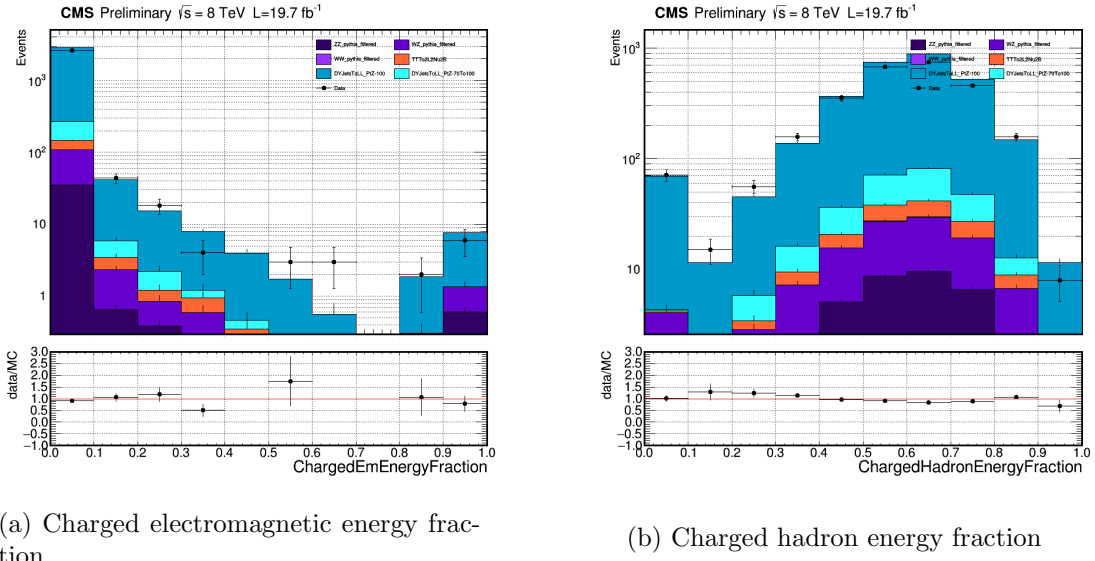


Figure 3-8: Charged electromagnetic/hadron energy fraction is defined by the ratio of the energy of charged particles in ECAL/HCAL to the jet energy.

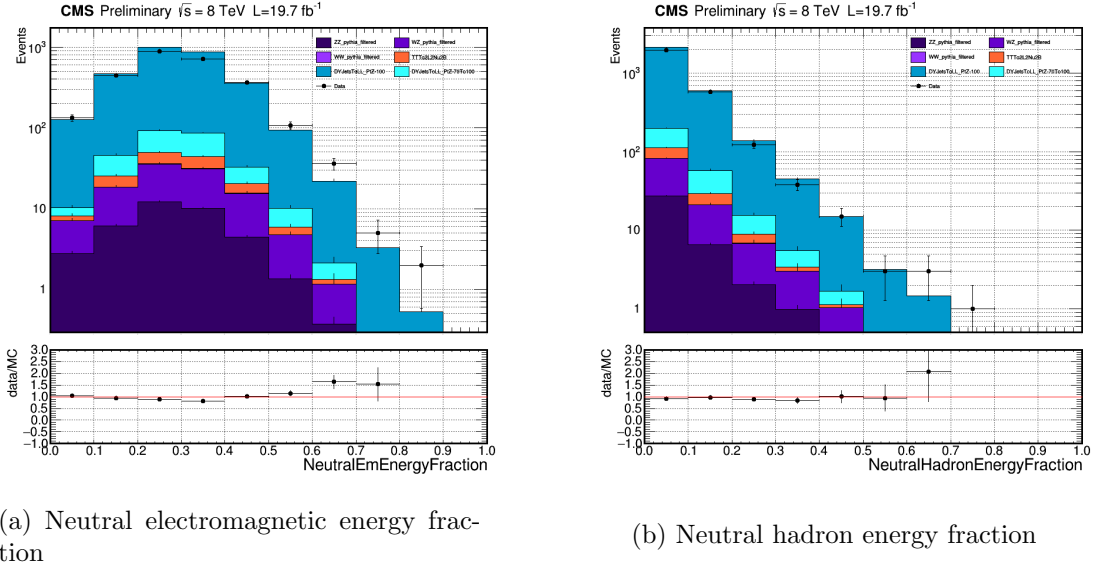


Figure 3-9: Neutral electromagnetic/hadron energy fraction is defined by the ratio of the energy of neutral particles in ECAL/HCAL to the jet energy.

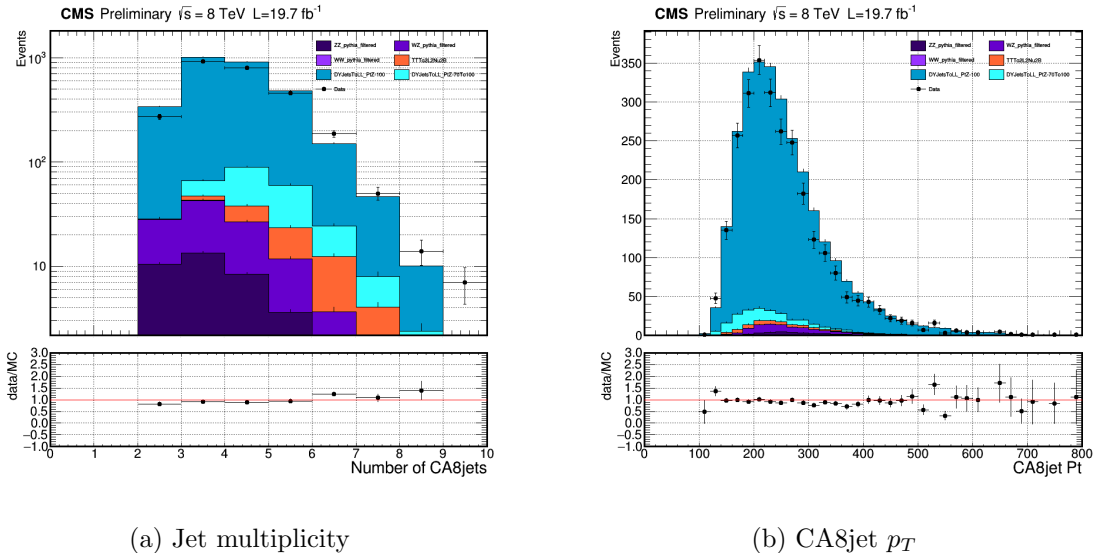


Figure 3-10: Comparison between data and MC in SB region using jet multiplicity (number of jets) and CA8jet transverse momentum.

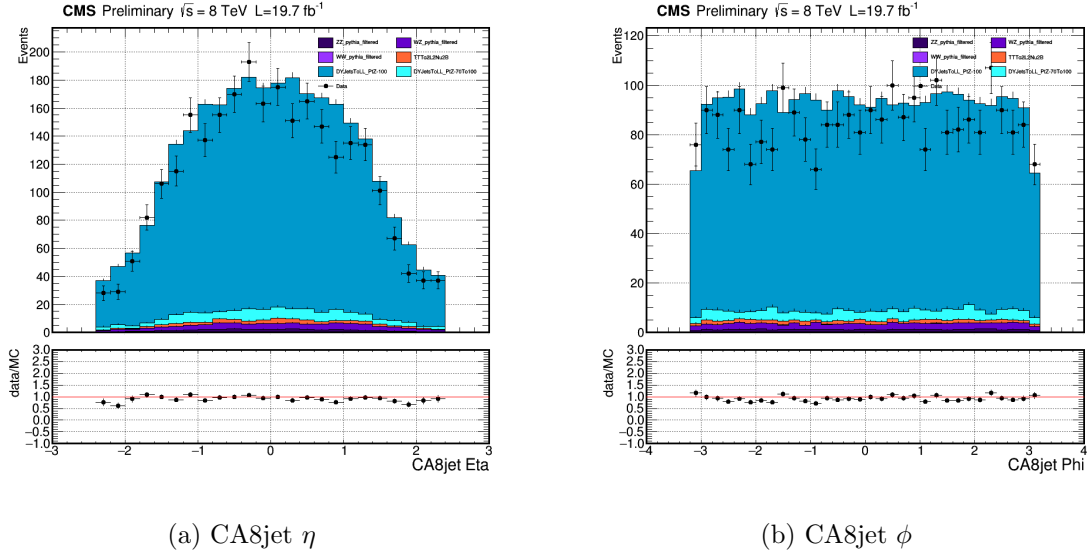


Figure 3-11: Comparison between data and MC in SB region using CA8jet η and ϕ .

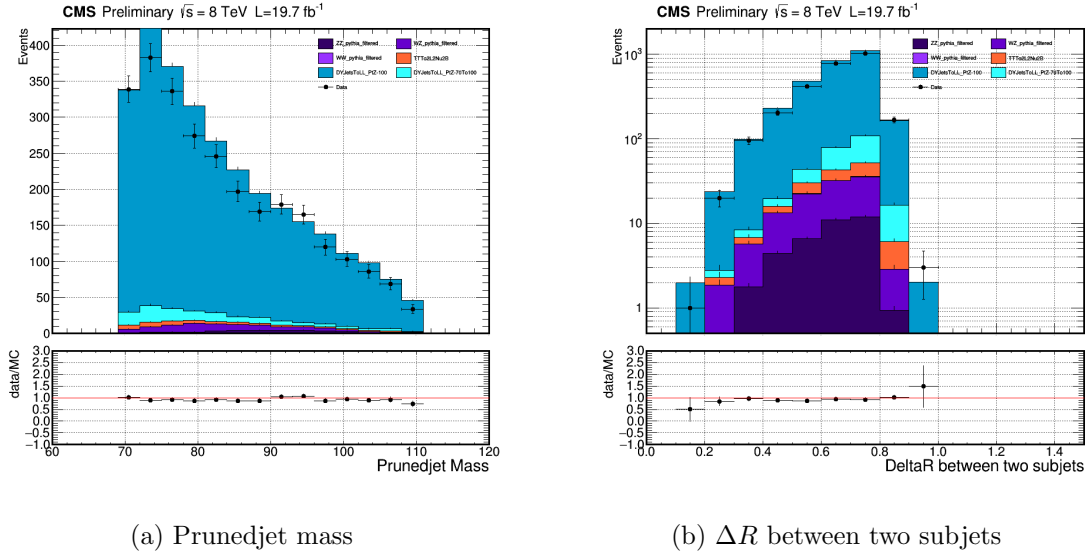


Figure 3-12: Left: the prunedjet mass in the SB region. Right: the spatial distance between two subjets within the CA8jet.

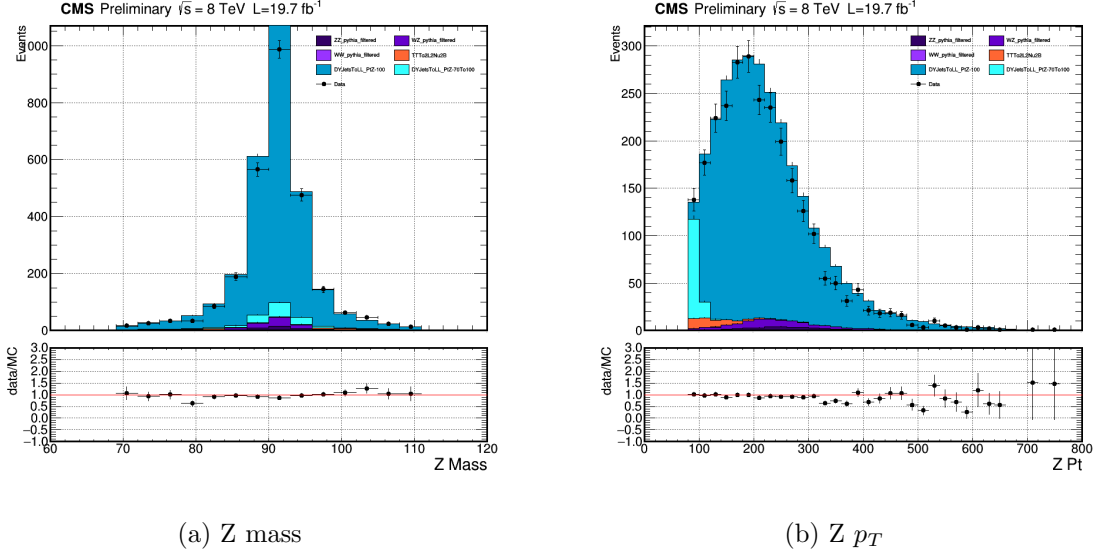


Figure 3-13: Comparison between data and MC in SB region using mass and transverse momentum of reconstructed Z boson.

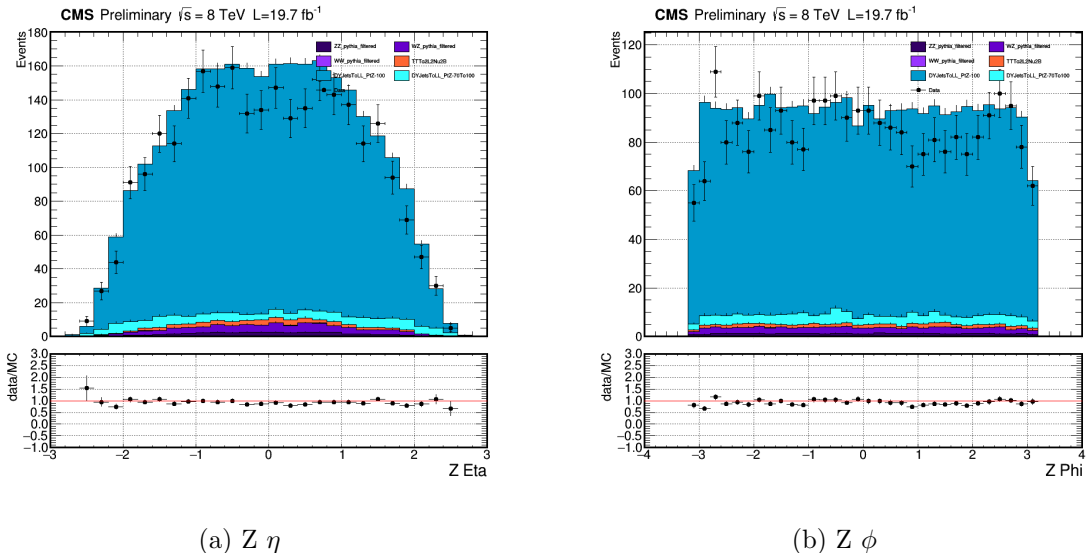


Figure 3-14: Comparison between data and MC in SB region using η and ϕ of reconstructed Z boson.

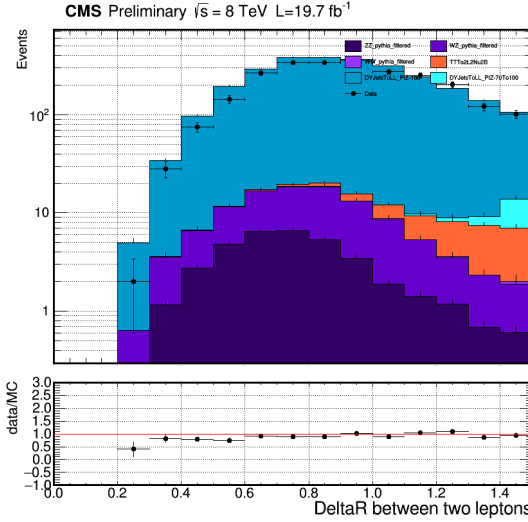


Figure 3-15: ΔR between the two selected leptons.

3.7 Background Estimation

The final aim of this analysis is to test the Z' hypothesis with the observed data, it is important to elaborate a trustworthy strategy for the SM background estimation. Despite the good description of the event kinematics provided by the MC simulation, it is more advisable to minimize the dependence on the MC and develop a data driven strategy.

3.7.1 α ratio method

α ratio is a data driven method in order to estimate the final background in data signal region. We consider the m_{Zh} MC mass spectrum in the SR and SB, then a ratio $\alpha(m_{Zh})$ of the two is created. This factor α allows prediction of the mass spectrum in the signal region starting from the observed distribution in the sidebands. Under the assumption that this extrapolation from the sidebands to the signal region works in the same way both for data and MC, we can estimate the final background distribution in data signal region by multiplying the m_{Zh} mass spectrum observed in the sidebands by this α ratio:

$$N_{SR}^{data}(m_{Zh}) = N_{SB}^{data}(m_{Zh}) \times \frac{N_{SR}^{MC}(m_{Zh})}{N_{SB}^{MC}(m_{Zh})} \equiv N_{SB}^{data}(m_{Zh}) \times \alpha(m_{Zh}) \quad (3.4)$$

638 We divided the spectrum in 14 non-uniform width bins, as shown in Table 3.7,
639 accordingly to the decreasing statistics in the high mass tail.

Bin	GeV
1	[680, 720]
2	[720, 760]
3	[760, 800]
4	[800, 840]
5	[840, 920]
6	[920, 1000]
7	[1000, 1100]
8	[1100, 1250]
9	[1250, 1400]
10	[1400, 1600]
11	[1600, 1800]
12	[1800, 2000]
13	[2000, 2200]
14	[2200, 2400]

Table 3.7: Binning of the Zh invariant mass range.

640 Finally, we multiplied the α ratio to the sidebands data m_{Zh} distribution and
641 obtained the prediction number of backgrounds in data signal region.

642 3.8 Signal Yields

643 Since all selections have been settled, we can look at the data in the signal region now.
644 In this section, signal efficiency and distributions of variables in SR will be reported.

645 3.8.1 signal efficiency

646 The signal efficiency is defined by the fraction of the number of events passing final
647 selection and the number of generated events in the signal MC samples (number of
648 generated events are shown in Table. 3.1).

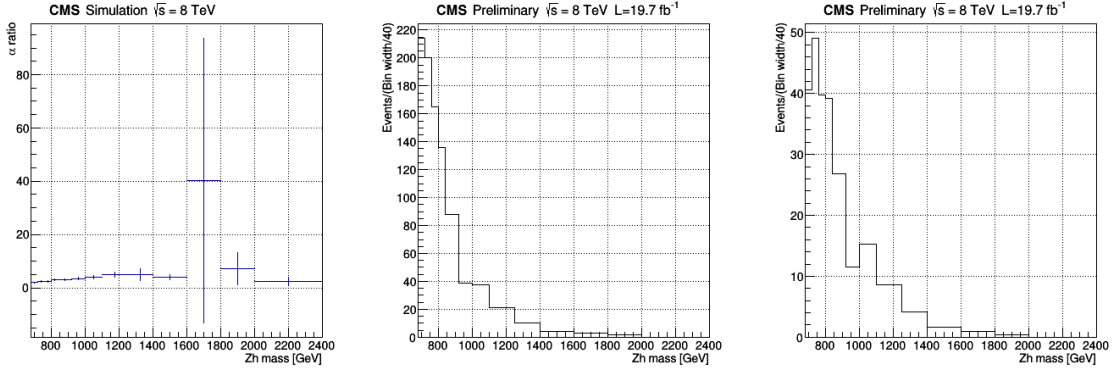


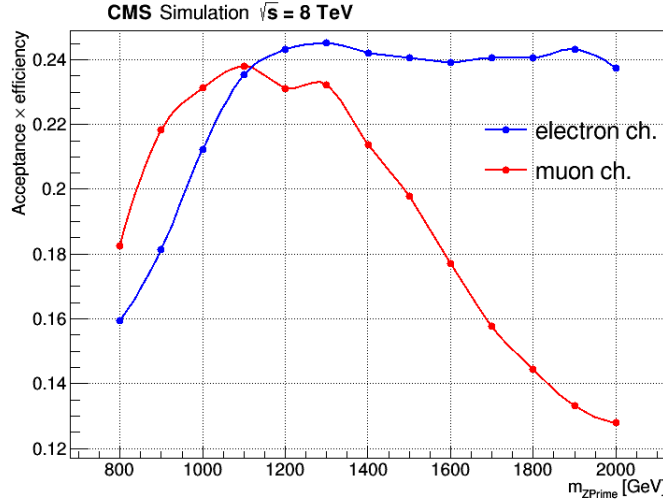
Figure 3-16: Left figure: the α ratio from MC simulation. Central figure: the m_{Zh} distribution observed from data SB. Right figure: the predicted m_{Zh} distribution in data signal region.

$$\epsilon_{SIG} \equiv \frac{\text{Number of events passing the final selections}}{\text{Number of generated events}} \quad (3.5)$$

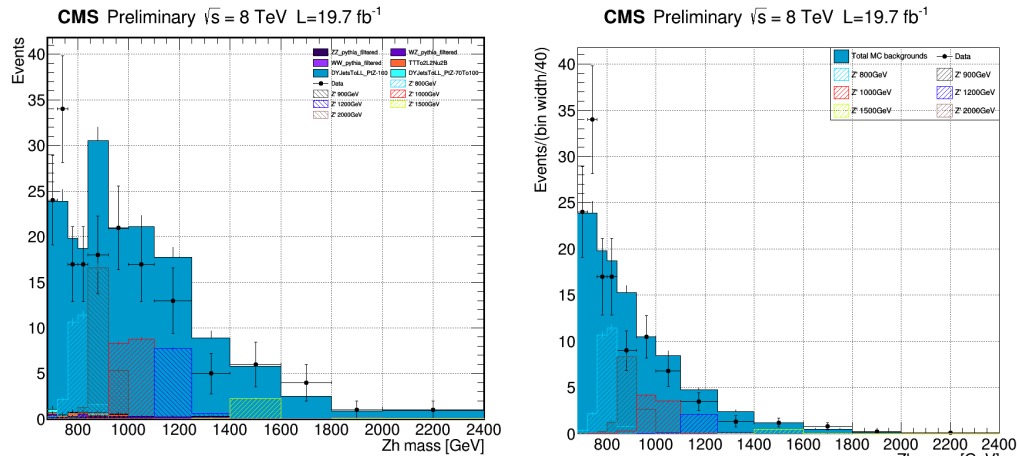
649 The result of efficiencies are shown in Fig. 3-17 (a). The figure shows a drop of
 650 efficiency in muon channel after signal mass of 1100 GeV, which comes from the muon
 651 isolation selection. It suggests the defect of the isolation definition. The isolation
 652 definition and its efficiency will be improved in the 13 TeV analysis.

653 3.8.2 The m_{Zh} spectrum

654 The Z' is reconstructed by combining the four-momentum of selected Z boson and
 655 leading jet. A comparison between data and MC of the reconstructed Zh invariant
 656 mass distribution in the signal region is shown in Fig. 3-17 (b)(c). Inspecting the SR
 657 mass distributions, one can see that data do not present any significant excess from
 658 the MC expectation, so we decide to put limits on the production cross section times
 659 the branching ratio for the $Z' \rightarrow Zh$ process. This Zh invariant mass spectrum will be
 660 used for computing the limit as shape information. Furthermore, in the last chapter,
 661 the number of events in the signal yields will be used for cut and count method to
 662 set the limits.



(a) Signal efficiencies for each Z' samples



(b) m_{Zh} spectrum

(c) m_{Zh} spectrum (normalized bin width)

Figure 3-17: (a) The signal efficiencies plot of each Z' mass point. (b) Invariant mass distribution of the MC background simulation compared to the observed data and MC signal shape in the SR. (c) Normalized bin width m_{Zh} distribution (bin width/bin width of the first bin).

663 3.8.3 The CSV distribution

664 Despite the reconstructed Zh mass as shape information, we introduced another pow-
 665 erful variable to discriminate signal from background. The overall branching ratio for
 666 a SM Higgs decaying into $b\bar{b}$ is about 56% and for Higgs decaying into two quarks
 667 only, the $\text{BR}(h \rightarrow b\bar{b})$ is about 95% [52]. Therefore, the b-tagging CSV working point
 668 is a power tool for searching this channel.

669 Although the recommend CSV selection (loose working point) from BTV group
 670 [51] for the boosted Higgs decay result in very low effiency for both background
 671 and signal MC samples. Instead of taking selection on the CSV, we use the overall
 672 distribution as another source of shape information to set the limits. The method
 673 how we retrive the CSV distribution is shown in Table. 3.8.

Category	BTV recommend (CSVL)	Modified
If $\Delta R_{subjets} > 0.3$	subjet CSV > 0.244	use the subjets CSV shape directly
If $\Delta R_{subjets} < 0.3$	CA8jet CSV > 0.244	use the CA8jet CSV shape directly

Table 3.8: The recommend selection from BTV group for boosted Higgs decay. If the ΔR between the two subjets within CA8jet larger than 0.3, applying CSVL selection on both subjets. If $\Delta R_{subjets} < 0.3$, appliny CSVL on the CA8jet. In this analysis, we use the overall CSV distributions instead of selecting events by this variable (Modified). Note that, only leading CA8jet (the Higgs candidate) and subjets within it are considered in this strategy.

674 The comparison of the CSV distributions between simulation background, signal
 675 and data is shown in Fig. 3-18. Note that, the area of each distribution is set to one
 676 in order to compare the shape difference. Inspecting Fig. 3-18, signal shapes tend to
 677 distribute on the right side while the backgrounds tend to be on the left, which shows
 678 the discriminating power of CSV variable. We only report and use the distribution
 679 from the $\Delta R > 0.3$ category to set the final limits because of lack of statics in the
 680 CA8jet CSV case. The higher CSV score means the subjet acts more like a b-jet.

681 Finally, we combine the CSV and the Zh mass distribution, making 2D histograms.
 682 Results of MC backgrounds, signal and data are shown in next pages.

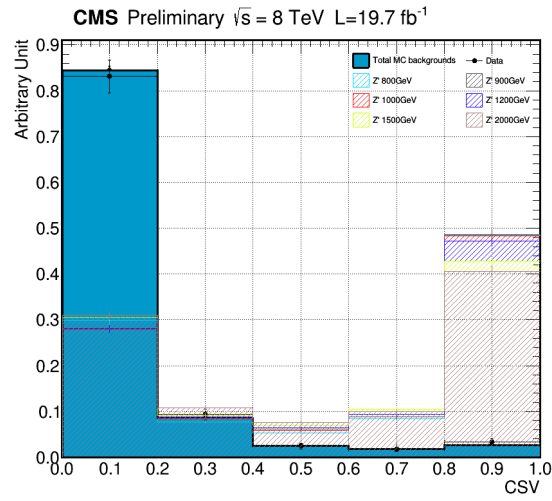


Figure 3-18: The CSV distribution comparison between data and MC samples in SR.

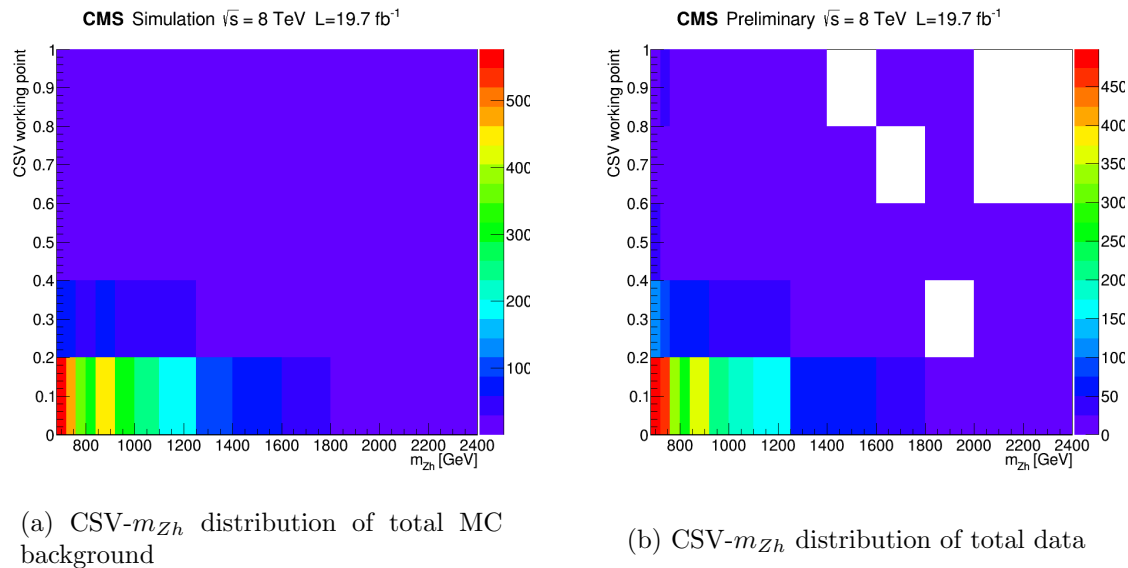


Figure 3-19: The combined 2D shape result of data and MC background in SR.

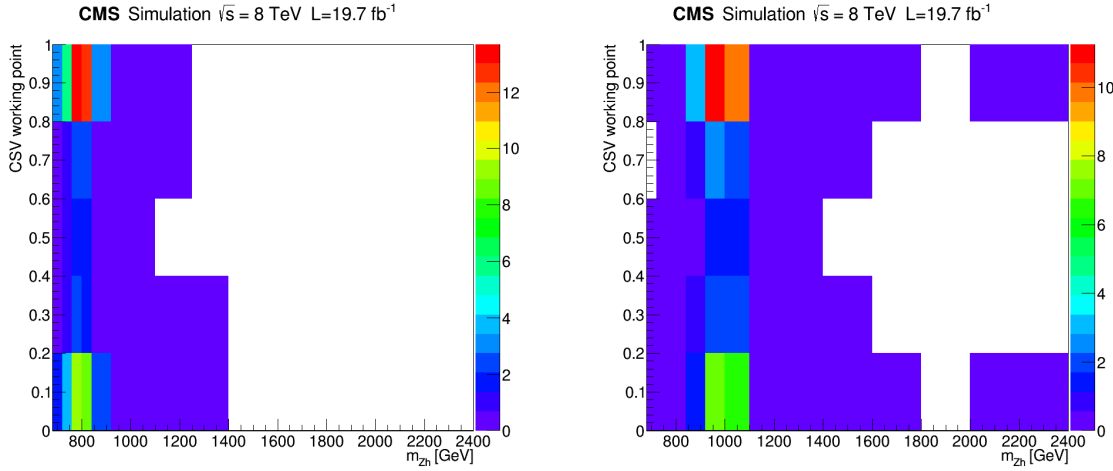


Figure 3-20: The combined 2D shape result in SR of 800 GeV and 1000 GeV signal MC samples.

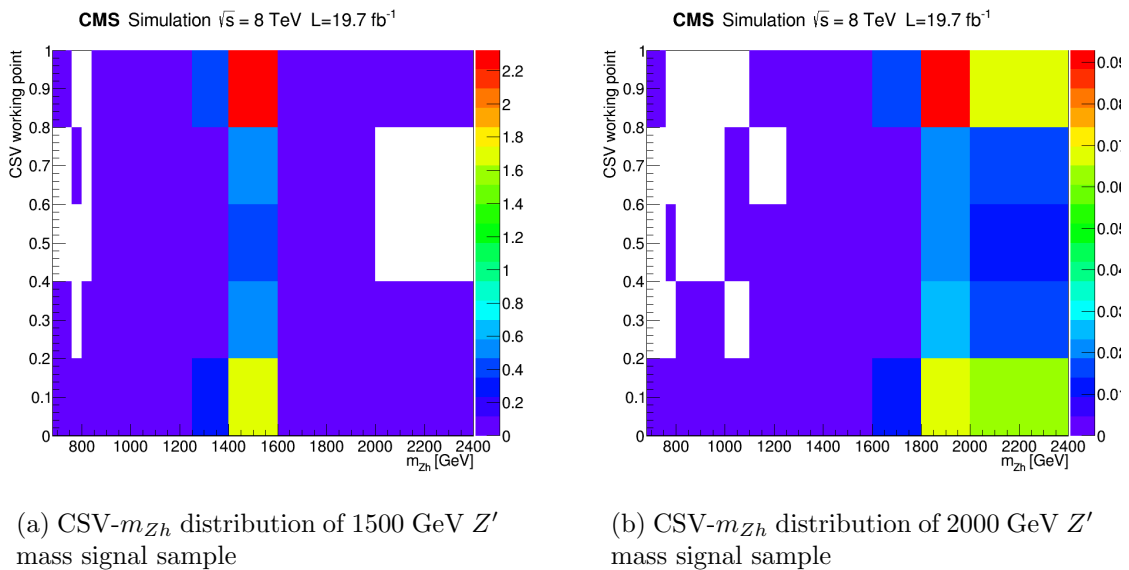


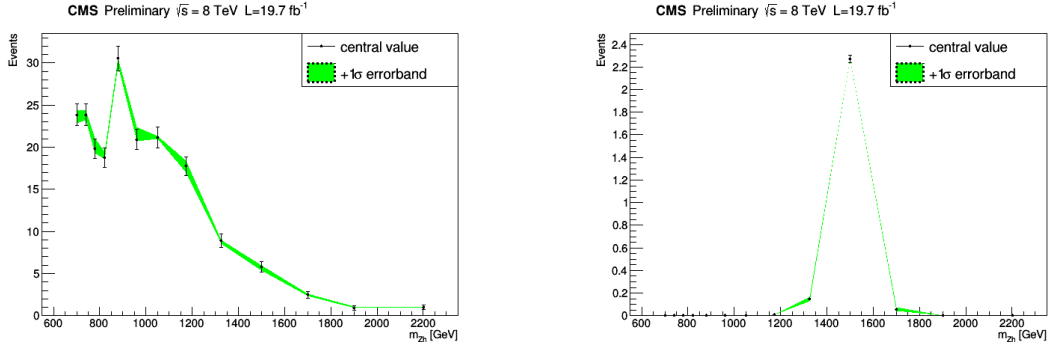
Figure 3-21: The combined 2D shape result in SR of 1500 GeV and 2000 GeV signal MC samples.

683 3.9 Systematic uncertainties

684 The background and signal predictions are affected by systematic uncertainties that
 685 have to be estimated and taken into account for limit setting. This section includes
 686 a list of the relevant systematic uncertainties for this analysis and how they are
 687 estimated.

688 • **Luminosity:** The overall uncertainty of the LHC luminosity delivered to CMS
 689 in the 2012 Run-I is measured to be 2.6% [53]

690 • **Jet energy scale:** The systematic on the jet energy scale was studied by scaling
 691 up and down the jet mass and p_T according to the uncertainty associated to
 692 the jet energy corrections used. The Zh mass distributions reconstructed by jet
 693 four-momentum is affected and therefore we consider the shape uncertainty as
 694 well, shown in Fig. 3-22. The overall uncertainty is about 8%.



(a) The systematic uncertainty of jet energy scale on background MC m_{Zh} spectrum.

(b) The systematic uncertainty of jet energy scale on signal MC m_{Zh} spectrum.

Figure 3-22: SR m_{Zh} distributions for both signal (1500 GeV) and background MC samples. The uncertainty of jet energy scale is shown as the green error band ($\pm 1\sigma$), while the error bar presents the statistic error.

695 • **CSV distribution normalization:** The uncertainty comes when normalizing
 696 the CSV distributions of MC background prediction in order to match the data
 697 distribution, which is estimated about 10%.

- 698 • **Pile-up reweighting:** As described previously in section 3.4, we reweight the
 699 pile-up interactions in MC predictions for better modeling. To calculate the
 700 uncertainties on the pile-up simulation, we produce two pile-up distributions
 701 where the minimum bias cross section is shifted by $\pm 5\%$ [54]. The impact on
 702 the event yields is about 2%. Despite the effects are small, we still consider it
 703 as the shape uncertainty. Fig. 3-23 shows the variation distributions of number
 704 of vertices for $\pm 1\sigma$.

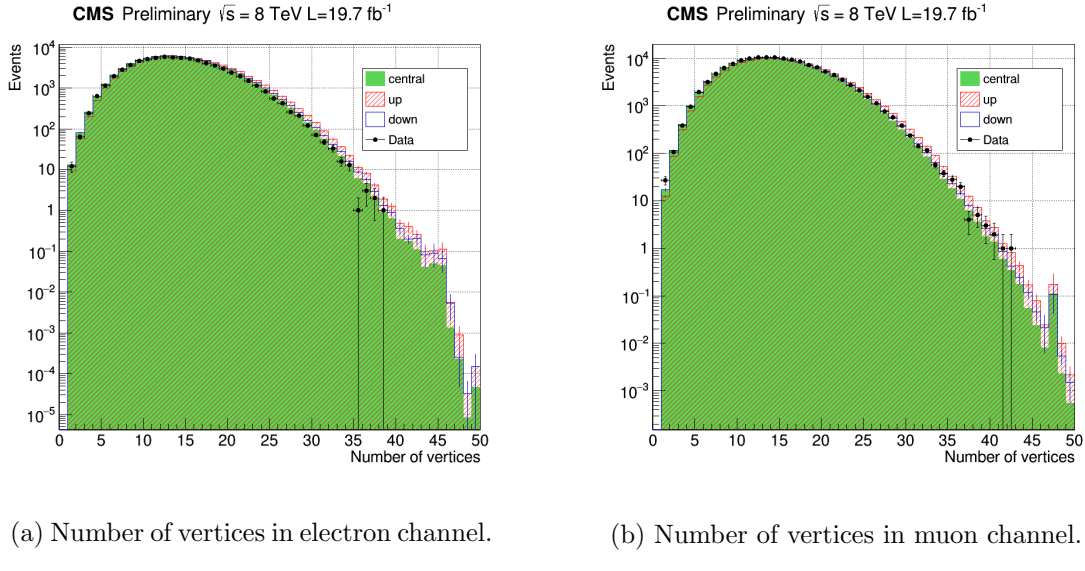


Figure 3-23: (a) shows the distributions of number of vertices in electron channel, comparing central value of the total background prediction and the $\pm 1\sigma$ variation, and data as well. (b) shows the result in muon channel.

- 705 • **Lepton ID scale factor:** The muon/electron ID scale factor depends on the
 706 kinematics of muon/electron (Table. 3.9). This systematic was studied by ap-
 707 plying $\pm 1\sigma$ to the scale factor, the estimated uncertainty is 0.08% for signal
 708 yields, 0.1% for the Z+jets background, 0.05% for $t\bar{t}$, and 0.06% for the SM
 709 diboson backgrounds. No shape uncertainties are considered.
- 710 • **b-jet Ratio:** Since the Drell-Yan process also generates b-jets into our back-
 711 ground, the uncertainty of production cross section of Z+b-jets events indeed

affects the number of background yield. The cross section ratio defined as σ_{Z+bjet} divided by σ_{Z+jet} and its uncertainties have been studied in [55]. By scaling 1σ on the ratio, we estimated there's 0.2% uncertainty for our Z+jets background yield.

- **SHERPA:** The major background sample in this analysis is Z+jets, which is generated by MADGRAPH and showered by PYTHIA. In order to study the dependence on the MC generator, we use the Z+jets sample generated by SHERPA [56] to estimate the background yield again. The relative uncertainty between SHERPA and MADGRAPH×PYTHIA from the estimated background yield is taken as the systematic by 12%.
- **Diboson cross section:** Uncertainties of the SM WW/WZ/ZZ production cross section affect their estimated background yield about 5.4%/6.7%/5.5%.
- **PDF uncertainty:** Systematic uncertainties coming from different choice of PDF sets have been considered for this analysis. This study is performed by varying the PDF set when producing the signal samples. The default PDF set we used is CTEQ6L1, replaced by the following PDF set: MSTW2008lo, MSTW2008nlo, NNPDF21_lo, NNPDF21_nlo and CT10. Comparison of distributions from different PDF sets are shown in Fig. 3-24. The estimated overall uncertainty for signal yields is 12% (maximum), shape uncertainty is also taken into account.

electron p_T [GeV]	$0.0 < \eta < 0.8$	$0.8 < \eta < 1.442$	$1.556 < \eta < 2.0$	$2.0 < \eta < 2.5$
20-30	1.005 ± 0.003	0.981 ± 0.003	0.980 ± 0.005	1.017 ± 0.006
30-40	1.004 ± 0.001	0.991 ± 0.001	0.992 ± 0.002	1.019 ± 0.003
40-50	1.008 ± 0.001	0.994 ± 0.001	1.004 ± 0.002	1.005 ± 0.001
50-200	1.008 ± 0.001	0.999 ± 0.001	1.006 ± 0.003	1.009 ± 0.002
muon p_T [GeV]	$0.0 < \eta < 0.8$	$0.8 < \eta < 2.1$	$2.1 < \eta < 2.4$	
20-40	1.0043 ± 0.0004	1.0074 ± 0.0005	1.022 ± 0.001	
40-100	1.0012 ± 0.0004	1.0043 ± 0.0004	1.014 ± 0.001	

Table 3.9: Data to simulation scale factors for muon and electron identification requirements in various p_T and η ranges.

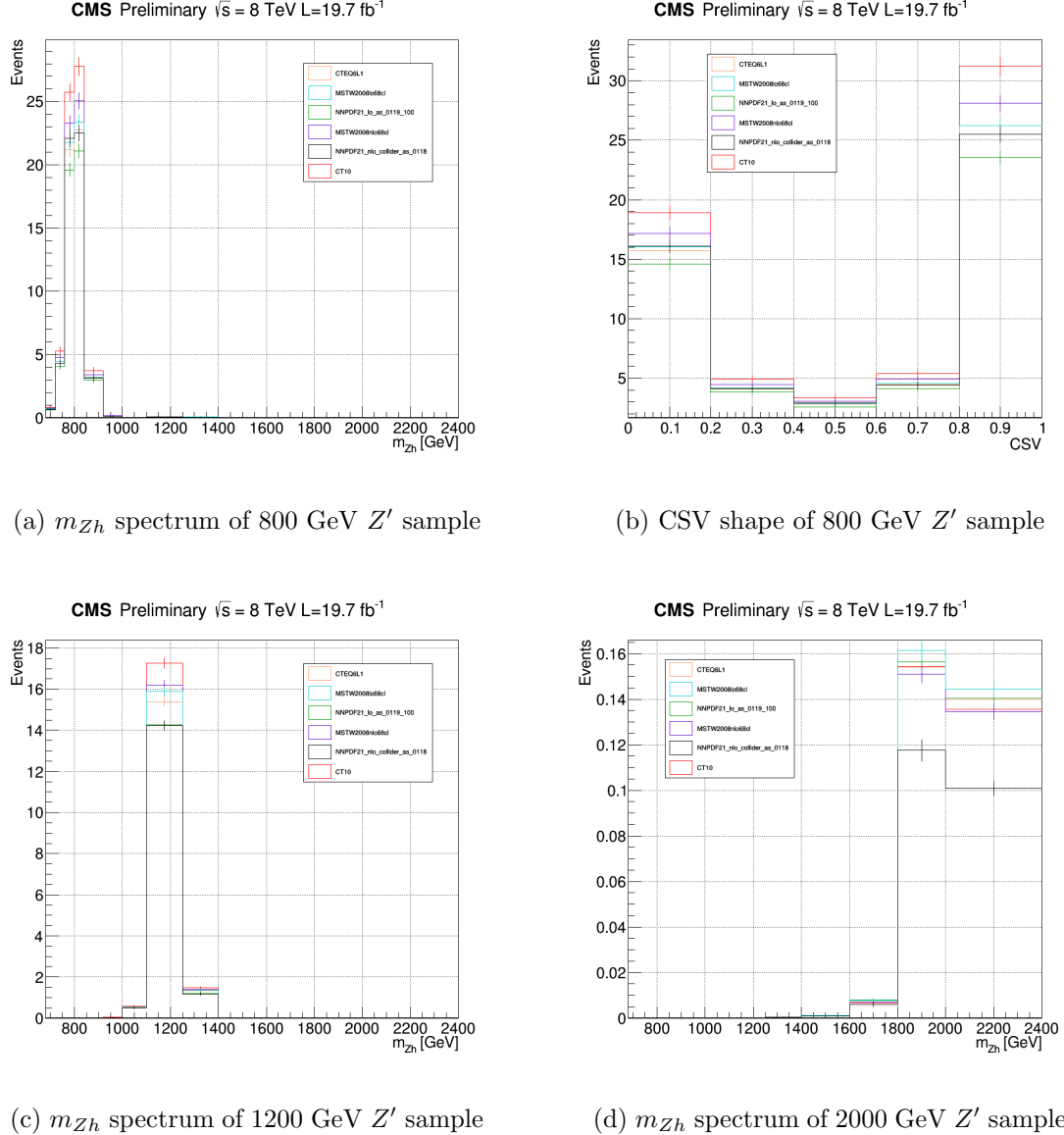


Figure 3-24: The comparison between different PDF sets using m_{Zh} spectrum and CSV variable.

732 **Chapter 4**

733 **Results and conclusion**

734 In this chapter, the signal, background and data yields after applying full selections
735 are used to determine the upper limits of the production cross section of Z' . The
736 95% confidence-level limit on the signal contribution in the data is computed by
737 the CL_s method [57, 58] with the RooStats [59] package. In order to extract the
738 limit on the production cross section times the branching ratios, the CMS standard
739 combination tool [60] has been used. Moreover, the Asymptotic method is used
740 to calculate preliminary 95% C.L. upper limits with 1σ and 2σ bands using the
741 CL_s frequentist calculation currently recommended by the LHC Higgs Combination
742 Group.

743 **4.1 Exclusion limit results**

744 **4.1.1 Counting result**

745 The expected exclusion limits with the ± 1 and $\pm 2 \sigma$ band, obtained by the provided
746 event yield information, are reported in Fig. 4-1 (a) in terms of upper limits on the
747 signal cross section.

748 **4.1.2 1D shape result**

749 In addition to the event yield information, the m_{Zh} distributions of predicted signal,
750 background and data are provided. All the statistical and systematics uncertainties
751 (with shape uncertainties) are included. The result is shown in Fig. 4-1 (b).

752 **4.1.3 2D shape result**

753 Both the CSV shape and the m_{Zh} spectrum are considered in this strategy. Therefore
754 the systematics related to the CSV shape are also introduced. The result is shown in
755 Fig. 4-1 (c).

756 **4.2 Conclusion**

757 Since no excess above the expected SM background was found, the result is interpreted
758 as an exclusion limit on the production cross section times the branching ratio in the
759 Zh channel as a function of the resonance mass.

760 Inspecting the limit result, the counting method shows no sensitivity on the cross
761 section limit plot. The expected (observed) lower bound on the Z' mass obtained in
762 the 1D limit result (top figure) is 1257 (1350) GeV, while the 2D result gives 1528
763 (1477) GeV. The 2D method has improved the limits significantly.

764 Finally, this analysis puts an upper limit at 95% confidence level on the cross
765 section of $pp \rightarrow Z' \rightarrow Zh$ at $\sqrt{s} = 8$ TeV. The maximal expected (observed) limit
766 result of 1528 (1477) GeV is determined.

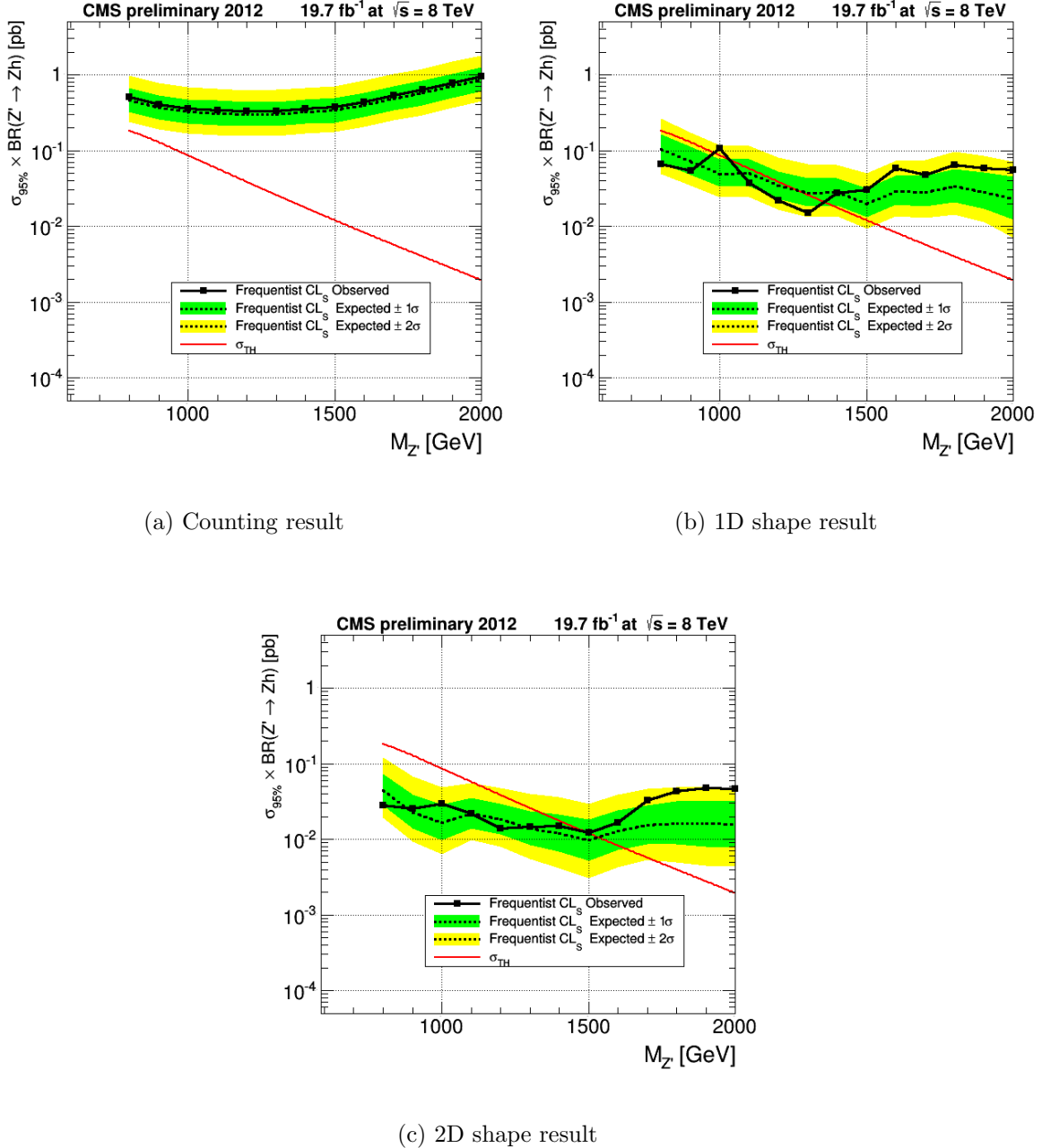


Figure 4-1: Observed and expected (with $\pm 1(2)\sigma$ band) 95% C.L. upper limit on $\sigma \times \text{BR}(Z' \rightarrow Z h)$ including all statistical and systematics uncertainties.

Bibliography

- [1] CMS Collaboration. Jet mass in di-jet and vector boson plus jet events. CMS Physics Analysis Summary CMS-PAS-SMP-12-019, CMS, 2012.
- [2] CMS Collaboration. Identification of b-quarks jets with the CMS experiment. *JINST*, 8:P04013, 2013.
- [3] ATLAS Collaboration. Observation of a new particle in the search for the Standard Model Higgs boson with the ATLAS detector at the LHC. *Phy. Lett. B*, 716:1, 2012.
- [4] CMS Collaboration. Observation of a new boson at a mass of 125 GeV with the CMS experiment at the LHC. *Phy. Lett. B*, 716:30, 2012.
- [5] CMS Collaboration. Observation of a new boson with mass near 125 GeV in pp collisions at $\sqrt{s} = 7$ and 8 TeV. *JHEP*, 06:081, 2013.
- [6] CMS Collaboration. Precise determination of the mass of the Higgs boson and tests of compatibility of its couplings with the standard model predictions using proton collisions at 7 and 8 TeV. *Eur. Phys. J. C*, 75:212, 2015.
- [7] ATLAS Collaboration. Measurement of the Higgs boson mass from the $H \rightarrow \gamma\gamma$ and $H \rightarrow ZZ^* \rightarrow 4l$ channels in pp collisions at center-of-mass energies of 7 and 8 TeV with the ATLAS detector. *Phys. Rev. D*, 90:052004, 2014.
- [8] ATLAS Collaboration. Evidence for the spin-0 nature of the Higgs boson using ATLAS data. *Phys. Lett. B*, 726:120, 2013.
- [9] CMS and ATLAS Collaboration. Combined Measurement of the Higgs Boson Mass in pp Collisions at $\sqrt{s} = 7$ and 8 TeV with the ATLAS and CMS Experiments. *Phys. Rev. Lett.*, 114:191803, 2015.
- [10] Mads T. Frandsen. Minimal Walking Technicolor. arXiv:0710.4333 [hep-ph], <http://arxiv.org/abs/0710.4333>, 2007.
- [11] T. Han, H. E. Logan, B. McElrath, and L.-T. Wang. Phenomenology of the little Higgs model. *Phys. Rev. D*, 67:095004, 2003.
- [12] M. Schmaltz and D. Tucker-Smith. LITTLE HIGGS THEORIES. *Annual Review of Nuclear and Particle Science*, 55:no. 1, 229–270, 2005.

- 796 [13] M. Perelstein. Little Higgs models and their phenomenology. *Progress in Particle*
 797 *and Nuclear Physics*, 58:no. 1, 247–291, 2007.
- 798 [14] R. Contino, D. Pappadopulo, D. Marzocca, and R. Rattazzi. On the effect of
 799 resonances in composite Higgs phenomenology. *Journal of High Energy Physics*,
 800 2011:no. 10, 1–50, 2011.
- 801 [15] D. Marzocca, M. Serone, and J. Shu. General composite Higgs model. *Journal*
 802 *of High Energy Physics*, 2012:no. 8, 1–52, 2012.
- 803 [16] B. Bellazzini, C. Csaki, and J. Serra. Composite Higgses. *Eur. Phys. J.*, C74:no.
 804 5, 2766, 2014.
- 805 [17] D. Pappadopulo, R. Torre A. Thamm, and A. Wulzer. Heavy vector triplets:
 806 bridging theory and data. *Journal of High Energy Physics*, 2014:no. 9, 1–50,
 807 2014.
- 808 [18] Andrea Wulzer. An Equivalent Gauge and the Equivalence Theorem.
 809 arXiv:1309.6055 [hep-ph], <http://arxiv.org/abs/1309.6055>, 2013.
- 810 [19] V. Barger, W.-Y. Keung, and E. Ma. Gauge model with light W and Z bosons.
 811 *Phys. Rev. D*, 22:727, 1980.
- 812 [20] Lisa Benato, Yu-Hsiang Chang, Ching-Wei Chen, Michele de Gruttola, Ra-
 813 man Khurana Ji-Kong Huang, Stefano Lacaprara, Yun-Ju Lu, Jacopo Pazzini,
 814 Maurizio Pierini, Henry Yee-Shian Tong, Jun-Yi Wu, Shin-Shan Eiko Yu, Marco
 815 Zanetti, and Alberto Zucchetta. Search for heavy resonances decaying into a vec-
 816 tor boson and a Higgs boson in the $(ll, l\nu, \nu\nu)b\bar{b}$ final state. CMS Note 2015/186,
 817 CMS, 2015.
- 818 [21] A. Benaglia. The CMS ECAL performance with examples. *JINST*, 09:C02008,
 819 2014.
- 820 [22] CMS HCAL Collaboration. Design, Performance, and Calibration of CMS
 821 Hadron-Barrel Calorimeter Wedges. CMS Note 2006/138, CMS, 2006.
- 822 [23] Victor Daniel Elvira. Measurement of the Pion Energy Response and Resolution
 823 in the CMS HCAL Test Beam 2002 Experiment. CMS Note 2004/020, CMS,
 824 2004.
- 825 [24] J. Brooke on behalf of the CMS Collaboration. Performance of the CMS Level-1
 826 Trigger. arXiv:1302.2469 [hep-ex], <http://arxiv.org/abs/1302.2469>, 2013.
- 827 [25] J. Alwall, R. Frederix, S. Frixione, V. Hirschi, F. Maltoni, O. Mattelaer, H.-S.
 828 Shaoand T. Stelzer, P. Torrielli, and M. Zaro. The automated computation of
 829 tree-level and next-to-leading order differential cross sections, and their matching
 830 to parton shower simulations. *JHEP*, 07:079, 2014.

- 831 [26] Torbjorn Sjostrand, Stephen Mrenna, and Peter Skands. PYTHIA 6.4 Physics
 832 and Manual. *JHEP*, 0605:026, 2006.
- 833 [27] Stefano Frixione, Paolo Nason, and Giovanni Ridolfi. The POWHEG-hvq manual
 834 version 1.0. arXiv:0707.3081 [hep-ph], <http://arxiv.org/abs/0707.3081>, 2007.
- 835 [28] S. Chatrchyan et al. Performance of CMS muon reconstruction in pp collision
 836 events at $\sqrt{s} = 7$ TeV. *JINST*, 7:P10002, 2012.
- 837 [29] Wolfgang Adam, Boris Mangano, Thomas Speer, and Teddy Todorow. Track
 838 Reconstruction in the CMS tracker. CMS Note 2006/041, CMS, 2006.
- 839 [30] CMS Collaboration. Baseline muon selections for Run-I.
 840 <https://twiki.cern.ch/twiki/bin/view/CMSPublic/SWGuideMuonId>.
- 841 [31] CMS Collaboration. Physics TDR volume I, The CMS Physics Technical Design
 842 R I. CERN-LHCC-2006-001, page 521pp, 2006.
- 843 [32] W. Adam, R. Frhwirth, A. Strandlie, and T. Todorov. Reconstruction of elec-
 844 trons with the gaussian-sum filter in the cms tracker at the lhc. *Journal of*
 845 *Physics G: Nuclear and Particle Physics*, 31(9):N9, 2005.
- 846 [33] CMS Collaboration. E/gamma Commissioning and physics deliverables.
 847 <https://twiki.cern.ch/twiki/bin/view/CMS/EgCommissioningAndPhysicsDeliverables>.
- 848 [34] CMS Collaboration. HEEP Electron ID and isolation.
 849 <https://twiki.cern.ch/twiki/bin/viewauth/CMS/HEEPElectronID>.
- 850 [35] T. S. Williams, D. Newbold, and C. Shepherd-Themistocleous. Modified isolation
 851 cuts for the selection of high p_T electrons from the decay of boosted Z bosons.
 852 CMS Note 2012/168, CMS, 2012.
- 853 [36] Wikipedia. Color confinement. https://en.wikipedia.org/wiki/Color_confinement.
- 854 [37] M. Cacciari, G. P. Salam, and G. Soyez. The anti- k_t jet clustering algorithm.
 855 *JHEP*, 04:063, 2008.
- 856 [38] M. Wobisch and T. Wengler. Hadronization corrections to jet cross section in
 857 deep-inelastic scattering. arXiv:9907280 [hep-ph], <http://arxiv.org/abs/9907280>,
 858 1999.
- 859 [39] CMS Collaboration. Commissioning of the Particle-Flow reconstruction in
 860 Minimum-Bias and Jet Events from pp Collisions at 7 TeV. CMS Physics Anal-
 861 ysis Summary CMS-PAS-PFT-10-002, CMS, 2010.
- 862 [40] Y.L. Dokshitzer et al. Better jet clustering algorithms. *JHEP*, 08:001, 1997.
- 863 [41] CMS Collaboration. A Cambridge-Aachen (C-A) based Jet Algorithm for
 864 boosted top-jet tagging. CMS Physics Analysis Summary CMS-PAS-JME-09-
 865 001, CMS, 2009.

- 866 [42] N.Saoulidou and E.Tziaferi. Performance of the Particle-Flow jet identification
 867 criteria using proton-proton collisions at = 8 TeV. CMS Note 2014/227, CMS,
 868 2014.
- 869 [43] CMS Collaboration. Jet Identification. <https://twiki.cern.ch/twiki/bin/viewauth/CMS/JetID>.
- 870 [44] P. Tran et al. Measurement of jet mass in V+Jets events. CMS Note 2012/137,
 871 CMS, 2012.
- 872 [45] A. Bonato, R. Gerosa, and et al. Identifying hadronically decaying W bosons
 873 merged into a single jet. CMS Note 2013/072, CMS, 2013.
- 874 [46] J. Thaler, D. Krohn, and L.T. Wang. Jet Trimming. *JHEP*, 100:242001, 2010.
- 875 [47] J.M. Butterworth et al. Jet substructure as a new Higgs search channel at the
 876 LHC. *PhysRevLett*, 100:242001, 2008.
- 877 [48] S. Ellis, C. Vermilion, and J. Walsh. Techniques for improved heavy particle
 878 searches with jet substructure. *Phys. Rev.*, D80:051501, 2009.
- 879 [49] S. Ellis, C. Vermilion, and J. Walsh. Recombination algorithms and jet sub-
 880 structure: Pruning as a tool for heavy particle searches. *Phys. Rev.*, D81:094023,
 881 2010.
- 882 [50] S. Chatrchyan et al. Studies of jet mass in di-jet and W/Z + jet events. *JHEP*,
 883 1305:090, 2013.
- 884 [51] CMS Collaboration. Performance of b tagging at $\sqrt{s} = 8$ TeV in multihjet, $t\bar{t}$
 885 and boosted topology events. CMS Physics Analysis Summary CMS-PAS-BTV-
 886 13-001, CMS, 2013.
- 887 [52] A. Denner, S. Heinemeyer, I. Puljak, D. Rebuzzi, and M. Spira. Standard Model
 888 Higgs-Boson Branching Ratios with Uncertainties. arXiv:1107.5909 [hep-ph],
 889 <http://arxiv.org/abs/1107.5909>, 2011.
- 890 [53] CMS Collaboration. CMS Luminosity Based on Pixel Cluster Counting - Summer
 891 2013 Update. CMS Physics Analysis Summary CMS-PAS-LUM-13-001, CMS,
 892 2013.
- 893 [54] CMS Collaboration. Estimating Systematic Errors Due to Pileup Modeling.
 894 <https://twiki.cern.ch/twiki/bin/view/CMS/PileupSystematicErrors>.
- 895 [55] CMS Collaboration. Measurement of the production cross sections for a Z boson
 896 and one or more b jets in pp collisions at $\sqrt{s} = 7$ TeV. *JHEP*, 06:120, 2014.
- 897 [56] T. Gleisberg, S. Hoeche, F. Krauss, M. Schoenherr, S. Schumann, F. Siegert,
 898 and J. Winter. Event generation with SHERPA 1.1. arXiv:0801.4622 [hep-ph],
 899 <http://arxiv.org/abs/0801.4622>, 2008.

- 900 [57] A. L. Read. Presentation of search results: the CL_s technique. *J.Phys.*, G28:2693,
901 2002.
- 902 [58] T. Junk. Confidence level computation for combining searches with small statis-
903 tics. *Nucl. Instrum. Meth.*, A434:435, 1999.
- 904 [59] L. Moneta. The RooStats Project. arXiv:1009.1003 [hep-ph],
905 <http://arxiv.org/abs/1009.1003>, 2010.
- 906 [60] CMS Collaboration. CMS Higgs Combine Tool.
907 <https://twiki.cern.ch/twiki/bin/view/CMS/SWGuideHiggsAnalysisCombinedLimit>.